Lyman Alpha Forest – Halo Cross – Correlations in Effective Field Theory

Anton Chudaykin[1, *] and Mikhail M. Ivanov[2, 3, †]

[1] *Département de Physique Théorique and Center for Astroparticle Physics, Université de Genève, 24 quai Ernest Ansermet, 1211 Genève 4, Switzerland*

[2] *Center for Theoretical Physics, Massachusetts Institute of Technology, Cambridge, MA 02139, USA*

[3] *The NSF AI Institute for Artificial Intelligence and Fundamental Interactions, Cambridge, MA 02139, USA*

We provide a perturbative effective field theory (EFT) description for anisotropic (redshift-space) correlations between the Lyman alpha forest and a generic biased tracer of matter, which could be represented by quasars, high-redshift galaxies, or dark matter halos. We compute one-loop EFT power spectrum predictions for the combined analysis of the Lyman alpha and biased tracers' data and test them on the publicly available high fidelity Sherwood simulations. We use massive and light dark matter halos at redshift $z = 2.8$ as proxies for quasars and high-redshift galaxies, respectively. In both cases, we demonstrate that our EFT model can consistently describe the complete data vector consisting of the Lyman alpha forest auto spectrum, the halo auto spectrum, and the Lyman alpha – halo cross spectrum. We show that the addition of cross – correlations significantly sharpens constraints on EFT parameters of the Lyman alpha forest and halos. In the combined analysis, our EFT model fits the simulated cross-spectra with a percent level accuracy at $k_{\rm max} = 1\ h{\rm Mpc}^{-1}$, which represents a significant improvement over previous analytical models. Thus, our work provides precision theoretical tools for full-shape analyses of Lyman alpha – quasar cross – correlations with ongoing and upcoming spectroscopic surveys.

I. INTRODUCTION

The Lyman alpha (Lyα) forest is a collection of absorption lines in the spectra of distant quasars produced by neutral hydrogen clouds in the intergalactic medium at redshifts $2 \lesssim z \lesssim 5$. Fluctuations in the flux transmitted through these clouds correlate with matter distribution on cosmological scales. The forest thus provides unique information about the large-scale structure of the Universe at high redshift, which has been extensively used to constrain the physics of neutrinos, dark matter, and dark energy [1–18]. In particular, the Lyα forest has been used for precision measurements of Baryon Acoustic Oscillations (BAO), periodic fluctuations in the matter density imprinted in the early universe[19–23].

The cosmological information from the Lyα forest can be significantly amplified by using correlations between the forest and high redshift quasars [22–25]. This includes both the BAO and the broadband shape of the Lyα forest correlations [26, 27], which have recently attracted a significant attention as a powerful complimentary probe. A theoretical challenge associated with this probe is an accurate modeling of Lyα forest – quasar cross-correlations, starting with the simplest two-point function and its Fourier transform, the power spectrum. While on the largest scales (wavenumbers $k \lesssim 0.1\ h{\rm Mpc}^{-1}$) the linear theory description of the Lyα forest – quasar power spectrum is adequate, it is expected to fail for larger wavenumbers, which still carry significant cosmological information. The non-linear Lyα forest – quasar correlations are challenging to model with hydrodynamical simulations because they require both large volumes and high resolution.

An inexpensive alternative to simulations is non-linear cosmological perturbation theory. While limited to scales $k \lesssim 1\ h{\rm Mpc}^{-1}$ where non-linear corrections are small, it provides a high level of accuracy and flexibility. The framework of effective field theory (EFT) for large-scale structure [28, 29] (see [30] for a recent review) provides a systematic program of building consistent perturbation theory based only on symmetries and dimensional analysis. EFT has recently become a standard tool to analyze the clustering of galaxies and quasars [31–36]. EFT for the Lyα forest has been developed in [37], which was based on the formalism of EFT for galaxies in the presence of selection effects [38]. Previous important perturbation theory studies of the Lyα forest include [39–43].

The main goal of this publication is to develop an EFT for the Lyα forest – quasar cross correlations. In EFT, different biased tracers of matter are described within the same effective bias expansion, such that the physi-

* anton.chudaykin@unige.ch
† ivanov99@mit.edu

cal differences between galaxies, quasars, and dark matter halos appear only in the values of bias parameters. Therefore, the EFT description that we lay out here is equally applicable for all these different tracers of matter. We will test our description against simulated Lyα – halo cross-correlations, in which we use light and massive halos as proxies for quasars and galaxies, respectively. Our work thus can be seen as an extension of ref. [43] that first studied the non-linear corrections to the Lyα – halo cross spectrum. Importantly, ref. [43] pointed out that linear theory becomes inadequate already on relatively large scales $\sim 0.3\ h\text{Mpc}^{-1}$, which motivates the development of a systematic non-linear model which we provide here.

Note that in contrast with usual biased tracers, EFT for the Lyα forest requires a different type of the bias expansion that accounts for the fact that the Lyα forest fluctuations are only symmetric w.r.t. rotations around the line of sight, as opposed to quasars or halos that enjoy the full three-dimensional rotational symmetry.

In addition to presenting the theory, we develop a full EFT-based pipeline for the combined analysis of the Lyα forest and halo auto-power spectra, as well as the Lyα – halo cross-correlation. In particular, we study the dependence of our result on the choices of the covariance matrices. Our pipeline can be readily applied to Lyα forest-quasar data from DESI [44, 45].

Our work is structured as follows. We outline our methodology and present the simulation data in Section II. There we give the details of the Lyα–halo cross spectrum calculated in effective field theory at the one-loop order. Our main results are summarized in Section III. Section IV draws conclusions and lists directions for future exploration. In Appendix A we present the results from the Lyα forest auto-power spectrum for various data cut choices. In Appendix B we introduce the extension of the EFT model which allows one to enhance the parameter constraints.

II. DATA AND METHODOLOGY

A. Data

We use the Sherwood suite of hydrodynamic simulations [46]. These are large publicly available high-resolution simulations of the intergalactic medium with up to 17.2 billion particles. The fiducial cosmology of these simulations is a flat ΛCDM model with $\Omega_m = 0.308$, $\Omega_b = 0.0482$, $\sigma_8 = 0.829$, $n_s = 0.961$, $h = 0.678$.

In this work, we present results from the largest simulation box `L160_N2048`, which has a box size of $L = 160\,h^{-1}\text{Mpc}$ and contains $N = 2048^3$ dark matter and gas particles. The simulations assume a homogeneous ionising background model, where the gas is in equilibrium and is optically thin [46]. Halo catalogs were generated with the friends of friends algorithm. In the main text, we focus on the snapshot at the redshift $z = 2.8$ which was previously analyzed in detail in ref. [43].

For the halo power spectrum, we consider two different samples: a catalog containing the most massive halos with $11.5 < \log_{10}(M/(h^{-1}M_\odot)) < 14$ and another catalog that contains all available halos. The first catalog is aimed to simulate the clustering properties of quasars, which are typically hosted by dark matter halos heavier than $10^{12}M_\odot$ [43]. Quasars of this type have been measured by the eBOSS collaboration and serve as a primary probe for DESI [34, 45]. The full halo catalog is dominated by significantly lighter halos, which act as proxies for high redshift galaxies that will be targeted by upcoming spectroscopic surveys such as Spec-S5 and WST. Indeed the Lyα emitters have $b_1 \simeq 1.5$ at $z \approx 3$ [47], very similar to the linear bias of our full halo catalog. We denote the catalogs of the most massive halos and all halos as H and LH, respectively. The halo number densities for these two catalogs at $z = 2.8$ are:

$$\begin{aligned} \text{Massive halos (H)}: \ \bar{n}_h^{-1} &= 188.61\,h^{-3}\text{Mpc}^3\,, \\ \text{Light halos (LH)}: \ \bar{n}_h^{-1} &= 0.37\,h^{-3}\text{Mpc}^3\,. \end{aligned} \tag{1}$$

The catalog of the massive halos has a lower number density, which results in a higher shot-noise value.

In this work, we utilize the 3D auto-power spectra of Lyα forest and halos, along with the Lyα – halo cross-power spectrum from [43]. The measurements are presented as a function of wavenumber k and the cosine of the angle between the corresponding Fourier mode and the line of sight μ. The k space is sampled by 20 log-spaced bins in the range $[k_F, k_{\text{Ny}}]$, where $k_F = 2\pi/L = 0.039$ is the fundamental mode of the box, and k_{Ny} is the Nyquist frequency. The μ is sampled by 16 uniformly spaced bins in the interval $[0, 1]$.

B. Methodology

We perform a Markov Chain Monte-Carlo analysis to sample from the posterior distribution of EFT parameters to access the performance of the EFT model. We

adopt a Gaussian likelihood defined as

$$-2\ln\mathcal{L}_P = (\boldsymbol{\mathcal{P}} - \boldsymbol{\mathcal{P}}_{\rm data})^t \cdot [\boldsymbol{\mathcal{C}}]^{-1} \cdot (\boldsymbol{\mathcal{P}} - \boldsymbol{\mathcal{P}}_{\rm data}) \ , \quad (2)$$

where $\boldsymbol{\mathcal{P}}$ and $\boldsymbol{\mathcal{P}}_{\rm data}$ represent the multi-dimensional theory and data vectors, respectively, and $\boldsymbol{\mathcal{C}}$ is the data covariance matrix. In the most general setup, the theory vector is composed of three different spectra,

$$\boldsymbol{\mathcal{P}} = (P^{\rm F}, P^{\rm H}, P^{\rm X}) \, , \quad (3)$$

where the uppercase indices "F", "H" and "X" correspond to the Lyα power spectrum, halo power spectrum, and the Lyα – halo cross spectrum, respectively. [1] These spectra are evaluated at the grid points (k_i,μ_i). We assume a Gaussian covariance matrix, whose linear theory expression is given by:

$$\boldsymbol{\mathcal{C}} = \begin{pmatrix} C^{\rm FF} & C^{\rm FH} & C^{\rm FX} \\ C^{\rm FH} & C^{\rm HH} & C^{\rm HX} \\ C^{\rm FX} & C^{\rm HX} & C^{\rm XX} \end{pmatrix} \, , \quad (4)$$

where each block represents a diagonal matrix defined as

$$\begin{aligned} C^{\rm FF}_{ii} &= 2N_i^{-1} P_i^{\rm F} P_i^{\rm F} \\ C^{\rm FH}_{ii} &= 2N_i^{-1} P_i^{\rm X} P_i^{\rm X} \\ C^{\rm FX}_{ii} &= 2N_i^{-1} P_i^{\rm F} P_i^{\rm X} \\ C^{\rm HH}_{ii} &= 2N_i^{-1} P_i^{\rm H} P_i^{\rm H} \\ C^{\rm HX}_{ii} &= 2N_i^{-1} P_i^{\rm H} P_i^{\rm X} \\ C^{\rm XX}_{ii} &= N_i^{-1} [P_i^{\rm X} P_i^{\rm X} + P_i^{\rm F} P_i^{\rm H}] \end{aligned} \quad (5)$$

In these expressions, N_i is a number of modes in the (k_i, μ_i) bin. This covariance structure introduces additional correlations between different spectra, which impose additional constraints on the inferred statistics. To assess the impact of these cross-correlations, we also perform an analysis with a diagonal covariance obtained by neglecting the off-diagonal terms: $C^{ab} = 0$ for $a \neq b$ where $a, b = \{\rm F, H, X\}$. This choice represents a more conservative approach, providing more flexibility in modeling the individual spectra. Additionally, it will allow us to validate the results obtained using the non-diagonal covariance, assessing its impact on the performance of the EFT model.

The individual power spectra P^a used in the covariance can either be extracted from data or predicted using a theoretical model. We found that the data measurements on large scales are affected by sample noise, which has a significant impact on the posterior distribution for bias parameters. [2] To achieve accurate covariance predictions, we employ a hybrid approach that combines the one-loop perturbation theory model with data measurements. In practice, we apply the following algorithm.

1. We compute the theoretical spectra P^a at the maximum point of the posterior in the range $k < k^a_{\rm max,\,fid}$, where $k^a_{\rm max,\,fid}$ denotes some fiducial configuration. For both individual and combined 3-spectra analyses, we use the values

$$(k^{\rm F}_{\rm max,\,fid}, k^{\rm H}_{\rm max,\,fid}, k^{\rm X}_{\rm max,\,fid}) = (2, 0.8, 1)\, h{\rm Mpc}^{-1} \ .$$

2. We construct the covariance matrix based on (4) and (5), using the one-loop theory predictions for $k < k^a_{\rm max,\,fid}$ and data measurements for $k > k^a_{\rm max,\,fid}$.

3. Using this covariance matrix, we perform an MCMC analysis with the fiducial data cuts.

This process is iterated until convergence, defined as a change of less than 1% in the bias parameter constraints. Upon achieving convergence, the covariance matrix corresponding to the fiducial data cuts is obtained. For arbitrary data cuts, the covariance matrix is constructed by combining the theoretical model for $k < k^a_{\rm max,\,fid}$ and data measurements for $k > k^a_{\rm max,\,fid}$. This approach ensures an accurate covariance prediction that remains robust on large scales while maintaining accuracy on small scales.

A comment on the Gaussian approximation is in order. While the Gaussian diagonal covariance provides a reliable measure of the statistical error it may be inaccurate on small scales, relevant for our analysis. Previous studies [48–50] showed that the Gaussian covariance for the galaxy power spectrum is highly accurate on mildly non-linear scales because the analysis is effectively dominated by the theoretical error introduced by marginalization over nuisance parameters [51–53]. While we expect the same argument to hold for the EFT of the Lyα forest, we note that, strictly speaking, it remains an assumption whose validation on different covariance

[1] The results of this section apply to both the massive halo and all-halo catalogs, which, for simplicity, we will collectively refer to as "H".

[2] This effect is more pronounced for the catalog of the most massive halos, whereas it is less important for the total halo catalog.

matrices (e.g. analytic vs. empirical covariance based on log-normal mocks) is left for future work. Therefore, we proceed with the covariance choices available to us, but caution that the interpretation of our results is contingent on the assumptions made about the covariance matrix.

Importantly, unlike [43] we do not introduce a noise floor when modelling the covariance matrices. This allows us to perform a more stringent test of the theoretical model, which precisely aims at extracting the information from large wavenumbers, which would be washed out by the noise floor.

C. Theoretical model

The theory vector $\boldsymbol{\mathcal{P}}$ is a one-loop EFT model that includes all necessary ingredients relevant on mildly non-linear scales. This is based on a perturbative expansion involving the most general operators that respect spacetime symmetries of the problem and the equivalence principle. The EFT-based model for the Lyα forest auto-power spectrum was formulated in [37] and later applied to the eBOSS 1D flux power spectrum of [54] in [55]. Here, we extend this approach by applying it to all three spectra: $P^{\rm F}$, $P^{\rm H}$, and $P^{\rm X}$. Note that our cross-correlation model has been recently applied to estimate the shift of the BAO peak in the quasar-Lyα cross spectra in [56]. We provide the details in this publication.

The general idea of our model is that the overdensity of halos, $\delta_{\rm H}$, and fluctuations of the Lyα flux, $\delta_{\rm F}$, individually can be perturbatively expanded over the linear matter density field. Without loss of generality, the non-linear density field δ_a with $a = \{{\rm F}, {\rm H}\}$ can be expressed at cubic order in the linear matter overdensity $\delta^{(1)}$ as

$$\begin{aligned}\delta_a(\mathbf{k}) = &\sum_{n=1}^{3}\Big[\prod_{j=1}^{n}\int\frac{d^3\mathbf{k}_j}{(2\pi)^3}\delta^{(1)}(\mathbf{k}_j)\Big]K_n(\mathbf{k}_1,...,\mathbf{k}_n)\\ &\times(2\pi)^3\delta_D^{(3)}(\mathbf{k}-\mathbf{k}_1-...-\mathbf{k}_j)\\ &-\sum_{n=0}^{2}c_{2n}^a\mu^{2n}k^2\delta^{(1)}(\mathbf{k})\\ &-\tilde{c}^aK_1(\mathbf{k})k^4f^4\mu^4\delta^{(1)}(\mathbf{k})+\varepsilon_a(\mathbf{k})\,,\end{aligned} \tag{6}$$

where K_n represent the EFT kernels, c_n are counterterms, $\tilde{c}$ is the higher-order counterterm needed to capture non-linear redshift space distortions of the collapsed tracer [31, 53, 57], and $\varepsilon_a(\mathbf{k})$ is the stochastic component uncorrelated with the linear density. The bias expansion is controlled by symmetries of the problem, so the K_n functions are different for halos and Lyα forest. For halos, the K_n are the standard redshift-space kernels, commonly used in EFT, see e.g. [31]. The Lyα forest introduce selection effects, leading to new line-of-sight dependent operators, specified in ref. [37]. The auto-power spectrum is defined as

$$\langle\delta_a(\mathbf{k})\delta_a(\mathbf{k}')\rangle = (2\pi)^3P^a_{\text{1-loop}}(k)\delta_D^{(3)}(\mathbf{k}+\mathbf{k}') \tag{7}$$

where $a = \{{\rm F}, {\rm H}\}$. For the cross spectrum, we write

$$\langle\delta_{\rm F}(\mathbf{k})\delta_{\rm H}(\mathbf{k}')\rangle = (2\pi)^3P^{\rm X}_{\text{1-loop}}(k)\delta_D^{(3)}(\mathbf{k}+\mathbf{k}') \tag{8}$$

We will use the following definition for the auto-power spectrum of the stochastic field $P_{\rm stoch}$:

$$\langle\epsilon_a(\mathbf{k})\epsilon_a(\mathbf{k}')\rangle = (2\pi)^3P^a_{\rm stoch}(k)\delta_D^{(3)}(\mathbf{k}+\mathbf{k}') \tag{9}$$

with $a = \{{\rm F}, {\rm H}\}$, and similarly for the cross-term $\langle\epsilon_{\rm F}(\mathbf{k})\epsilon_{\rm H}(\mathbf{k}')\rangle$, whose spectrum we denote $P^{\rm X}_{\rm stoch}$.

The anisotropic power spectra are calculated using the FFTLog approach embodied in the CLASS-PT code [58]. The details can be found in ref. [37, 59]. In our theory models, we use an approximate description of the non-linear damping of the BAO signal in the linear power spectrum by means of the isotropic damping factor derived in [60, 61]. Specifically, we apply the isotropic (real space) one-loop IR resummed formula from [61]. While it is straightforward to implement the full anisotropic suppression derived in [62], this is not required for our work given large statistical errors of the Sherwood data at the BAO wavenumbers $k \sim 0.1\ h{\rm Mpc}^{-1}$. In all expressions given below the one-loop IR resummation is assumed by default.

Below, we provide explicit expressions of the $P^{\rm F}$, $P^{\rm H}$, and $P^{\rm X}$ spectra individually. To avoid clutter, we will omit the uppercase index "F" for the EFT parameters and kernels associated with the Lyα forest auto-power spectrum.

1. *Lyα forest auto-power spectrum*

We start with the Lyα forest auto-power spectrum. In this case, the relevant operators are scalars under $SO(2)$ rotations around the line-of-sight. This implies a greater flexibility in the EFT bias expansion compared to the case of galaxies, leading to the new line-of-sight dependent operators, originally derived in [38]. By performing a direct calculation of eq. (7), we arrive at the one-loop

power spectrum for Lyα forest,

$$\begin{aligned} P^{\rm F}_{\text{1-loop}}(k,\mu) &= K_1^2(\mathbf{k})P_{\rm lin}(k) \\ &+ 2\int_{\mathbf{q}} K_2^2(\mathbf{q},\mathbf{k}-\mathbf{q})P_{\rm lin}(|\mathbf{k}-\mathbf{q}|)P_{\rm lin}(q) \\ &+ 6K_1(\mathbf{k})P_{\rm lin}(k)\int_{\mathbf{q}} K_3(\mathbf{k},-\mathbf{q},\mathbf{q})P_{\rm lin}(q) \\ &- 2(c_0+c_2\mu^2+c_4\mu^4)K_1(\mathbf{k})k^2P_{\rm lin}(k)\,. \end{aligned} \tag{10}$$

The linear EFT kernel is expressed as

$$K_1 = b_1 - b_\eta f\mu^2 \tag{11}$$

where b_1 is the selection-free linear bias and b_η is the new selection-dependent bias parameter. The K_2 and K_3 introduce new selection-dependent EFT operators which are absent in the case of galaxies. Explicit expressions for these non-linear operators are provided in ref. [37]. Next, the $k^2P_{\rm lin}$ corrections accounts for the higher-derivative contributions. The main role of these terms is to absorb the UV dependence of the loop integrals. Although these nominally contribute at the three-loop order and could be ignored at the 1-loop level, the inclusion of these parameters noticeably improves the fit [37], so we opted to retain c_i. Finally, we neglect the stochastic contributions. The physical stochastic contributions are strongly suppressed due to high column densities of the Lyα forest [63]. Note that in EFT non-zero stochasticity parameters are expected to be generated by the UV parts of loop integrals, but their effect is of the order of two-loop corrections at $z\approx 3$, see [56] for a detailed discussion and explicit tests.

The 1-loop EFT model for $P^{\rm F}$ depends on 16 free parameters: 2 linear biases, 11 non-linear biases and 3 higher-derivative operators. We impose the following priors on these parameters,

$$\begin{aligned} &b_1\in[-2,2]\,,\quad b_\eta\in[-2,2]\,,\quad b_2\sim\mathcal{N}(0,2^2)\,,\\ &b_{\mathcal{G}_2}\sim\mathcal{N}(0,2^2)\,,\quad b_{\Gamma_3}\sim\mathcal{N}(0,1^2)\\ &b_{\eta^2}\sim\mathcal{N}(0,2^2)\,,\quad b_{\delta\eta}\sim\mathcal{N}(0,2^2)\,,\\ &b_{(KK)_\parallel}\sim\mathcal{N}(0,2^2)\,,\quad b_{\Pi^{[2]}_\parallel}\sim\mathcal{N}(0,2^2)\,,\\ &b_{\Pi^{[3]}_\parallel}\sim\mathcal{N}(0,2^2)\,,\quad b_{\delta\Pi^{[2]}_\parallel}\sim\mathcal{N}(0,2^2)\,,\\ &b_{(K\Pi^{[2]})_\parallel}\sim\mathcal{N}(0,2^2)\,,\quad b_{\eta\Pi^{[2]}_\parallel}\sim\mathcal{N}(0,2^2)\,,\\ &\frac{c_{0,2,4}}{[h^{-1}\text{Mpc}]^2}\sim\mathcal{N}(0,1^2)\,, \end{aligned} \tag{12}$$

where $\mathcal{N}(\mu,\sigma^2)$ stands for a Gaussian distribution with mean μ and r.m.s. σ. Our analysis differs from the previous work [37] in several aspects. First, we include the cubic bias b_{Γ_3} because it affects the parameter error bars in the combined analyses. Second, we broaden the priors on the $c_{0,2,4}$, as we use a slightly different convention (10). Jumping ahead, let us note that we will find that the values of the higher-derivative parameters are of order 10^{-2} with errorbars that are much tighter than the priors. These values are consistent with the naturalness arguments that $c_i\sim k_{\rm NL}^{-2}$.

2. *Halo auto-power spectrum*

For the the halo power spectrum, we exploit the standard EFT model from [64]. This is based on a larger $SO(3)$ symmetry, which reduces a number of possible operators compared to the Lyman alpha forest case. In the absence of selection effects, the linear kernel takes the standard form,

$$K_1^{\rm H} = b_1^{\rm H} + f\mu^2 \tag{13}$$

where $b_1^{\rm H}$ denotes the linear halo bias.

The $P^{\rm H}$ model includes the stochastic contribution, which at 1-loop order is given by

$$P_{\rm stoch} = \frac{1}{\bar{n}_h}\left[1 + P^{\rm H}_{\rm shot} + a_0^{\rm H}\left(\frac{k}{k_{\rm NL}}\right)^2 + a_2^{\rm H}\mu^2\left(\frac{k}{k_{\rm NL}}\right)^2\right], \tag{14}$$

where $P^{\rm H}_{\rm shot}$ is residual constant shot-noise contribution, $a_0^{\rm H}$ and $a_2^{\rm H}$ are scale-dependent stochastic biases. We define the non-linear scale as $k_{\rm NL} = 3\,h{\rm Mpc}^{-1}$ following [37]. It should be noted that the constant shot-noise $\bar{n}_h^{-1}$ is subtracted from the halo auto-power spectrum data. The stochastic EFT parameters are expected to be $\mathcal{O}(1)$ numbers.

We also include a higher-order derivative correction, as the halos are virialized objects with significant velocities. Following [31], we incorporate the k^4 redshift-space counterterm,

$$P_{\nabla_z^4\delta}(k,\mu) = -\tilde{c}^{\rm H} f^4\mu^4k^4\left[K_1^{\rm H}\right]^2P_{\rm lin}(k) \tag{15}$$

where $\tilde{c}^{\rm H}$ is the higher-order counterterm.

The 1-loop EFT model for $P^{\rm H}$ features 11 EFT pa-

rameters. We adopt the following priors,

$$
\begin{aligned}
&b_1^{\rm H} \in [0,10]\,, \quad b_2^{\rm H} \sim \mathcal{N}(0,2^2)\,,\\
&b_{\mathcal{G}_2}^{\rm H} \sim \mathcal{N}(0,2^2)\,, \quad b_{\Gamma_3}^{\rm H} \sim \mathcal{N}(0,2^2)\\
&\frac{c_{0,2,4}^{\rm H}}{[h^{-1}{\rm Mpc}]^2} \sim \mathcal{N}(0,10^2)\,, \quad \frac{\tilde{c}^{\rm H}}{[h^{-1}{\rm Mpc}]^4} \sim \mathcal{N}(0,100^2)\\
&P_{\rm shot}^{\rm H} \sim \mathcal{N}(0,1^2)\,,\\
&a_0^{\rm H} \sim \mathcal{N}(0,1^2)\,, \quad a_2^{\rm H} \sim \mathcal{N}(0,1^2)\,,
\end{aligned}
\tag{16}
$$

For $b_1^{\rm H}$, $b_2^{\rm H}$, $b_{\mathcal{G}_2}^{\rm H}$ and $b_{\Gamma_3}^{\rm H}$ we adopt the same priors as in the $P^{\rm F}$ case (12). For the higher-derivative contributions, we choose large uninformative priors. The priors on stochastic bias parameters are motivated by the EFT naturalness arguments in the physical units [58].

It is important to note that in the combined 3-spectra analysis the $P^{\rm H}$ does not introduce new c_4 parameter. The equality of the $\mu^4 k^2 P_{\rm lin}$ counterterms for these two spectra, i.e. $c_4 = c_4^H$, is dictated by the equivalence principle [65, 66]. In this case, $P^{\rm H}$ introduces only 10 new EFT parameters. An extension of this model with a unique $\mu^4 k^2$ operator for the halo population is explored in Appendix B.

3. *Lyα – halo cross-power spectrum*

The computation of the Lyα – halo cross-power spectra (8) involves symmetrizing the expression with respect to the Lyα and halo tracers. The direct calculation lead us to the following expression,

$$
\begin{aligned}
&P^{\rm X}_{\text{1-loop}}(k,\mu) = K_1(\mathbf{k}) K_1^{\rm H}(\mathbf{k}) P_{\rm lin}(k)\\
&+ 2\int_{\mathbf{q}} K_2(\mathbf{q},\mathbf{k}-\mathbf{q}) K_2^{\rm H}(\mathbf{q},\mathbf{k}-\mathbf{q}) P_{\rm lin}(|\mathbf{k}-\mathbf{q}|) P_{\rm lin}(q)\\
&+ 3P_{\rm lin}(k)\int_{\mathbf{q}} [K_1(\mathbf{k}) K_3^{\rm H}(\mathbf{k},-\mathbf{q},\mathbf{q})\\
&+ K_1^{\rm H}(\mathbf{k}) K_3(\mathbf{k},-\mathbf{q},\mathbf{q})] P_{\rm lin}(q)\\
&- (c_0 + c_2\mu^2 + c_4\mu^4) K_1^{\rm H}(\mathbf{k}) k^2 P_{\rm lin}(k)\\
&- (c_0^{\rm H} + c_2^{\rm H}\mu^2 + c_4\mu^4) K_1(\mathbf{k}) k^2 P_{\rm lin}(k)\\
&+ P^{\rm X}_{\nabla_z^4\delta}\,.
\end{aligned}
\tag{17}
$$

Here we have used the fact that the $\mu^4 k^2$ operator is protected by the equivalence principle and is universal across all tracers.

A comment on the stochastic contribution is in order. In galaxy muti-tracer analysis it is often assumed that two types of galaxies have zero stochastic cross-correlation, see e.g. [67]. However, this assumption is hard to justify from the EFT point of view. For two tracers A and B one could in general write down [68]

$$
P^{\rm X}_{\rm shot}(k) = \frac{1}{\sqrt{\bar{n}_A \bar{n}_B}} + O(k^2/k^2_{\rm NL})\ . \tag{18}
$$

In our case effectively $\bar{n}^{-1}_{{\rm Ly}\alpha} \simeq 0$ [63], plus the number density of halos is quite high even for the massive ones, which makes $P^{\rm X}_{\rm shot}$ highly suppressed.

In EFT, however, $P^{\rm X}_{\rm shot}$ also contains the counterterm part needed to cancel the UV-dependence of the $\langle\delta^2\delta^2\rangle$ - type loop integrals. If we assume that the quadratic bias parameters are $O(1)$, this will give us the estimate [56]:

$$
P^{\rm X}_{\rm shot} \sim \frac{1}{k^3_{\rm NL}} \sim 0.05\ [h^{-1}{\rm Mpc}]^3\,. \tag{19}
$$

This will generate a non-zero $P^{\rm X}_{\rm shot}$, but its amplitude is very small given the error bars of the Sherwood simulation. Thus, we will proceed with $P^{\rm X}_{\rm shot} = 0$ in our main analyses, and use a model with non-zero $P^{\rm X}_{\rm shot}$ only to test the validity of our baseline analysis. Jumping ahead, let us say here that the addition of $P^{\rm X}_{\rm shot}$ does not improve the fit to the Sherwood data, and hence it is reasonable to set it to zero following our estimates. We note however, that for other tracers and experiments, e.g. eBOSS quasars with a large shot noise [34], one may need to include $P^{\rm X}_{\rm shot}$ in the fit.

We introduce only one unique operator for the cross-power spectrum, the next-to-leading order k^4 redshift-space counterterm. For this term, we employ a symmetrized version of (15),

$$
P^{\rm X}_{\nabla_z^4\delta}(k,\mu) = -\tilde{c}^{\rm X} f^4 \mu^4 k^4 K_1(\mathbf{k}) K_1^{\rm H}(\mathbf{k}) P_{\rm lin}(k) \tag{20}
$$

where $\tilde{c}^{\rm X}$ is a free EFT parameter. We ignore the stochastic contributions as they are expected to be negligible for the cross-power spectrum.

At face value, the 1-loop EFT model for $P^{\rm X}$ depends on 27 free parameters: 26 terms shared with the $P^{\rm F}$ and $P^{\rm H}$ models, and one unique FoG operator specific to the $P^{\rm X}$ spectrum. We impose the broad uninformative prior on the latter parameter,

$$
\frac{\tilde{c}^{\rm X}}{[h^{-1}{\rm Mpc}]^4} \sim \mathcal{N}(0,100^2)\,. \tag{21}
$$

D. Analysis pipeline

We fit the multidimensional vector $\boldsymbol{\mathcal{P}}$ (3) using the 1-loop EFT model. The theoretical calculation are carried

out with a custom script interfaced with the `CLASS-PT` code [58]. To sample the posterior distributions, we employ a Markov Chain Monte Carlo (MCMC) analysis.

We fix the cosmological parameters and vary only the EFT parameters. For example, in the combined 3-spectra analysis, we vary 27 nuisance parameters :

$$\{b_1, b_\eta, b_2, b_{\mathcal{G}_2}, b_{\eta^2}, b_{\delta\eta}, b_{(KK)_\parallel}, b_{\Pi^{[2]}_\parallel} | b_{\Gamma_3}, c_0, c_2, c_4, b_{\Pi^{[3]}_\parallel}, b_{(K\Pi^{[2]})_\parallel}, b_{\delta\Pi^{[2]}_\parallel}, b_{\eta\Pi^{[2]}_\parallel}\}$$
$$\times \{b_1^{\rm H}, b_2^{\rm H}, b_{\mathcal{G}_2}^{\rm H} | b_{\Gamma_3}^{\rm H}, c_0^{\rm H}, c_2^{\rm H}, \tilde{c}^{\rm H}, P_{\rm shot}^{\rm H}, a_0^{\rm H}, a_2^{\rm H}\} \times \{\tilde{c}^{\rm X}\}$$

The parameters on the left side of the vertical line are directly sampled in our MCMC chains, while the parameters on the right, which appear quadratically in the likelihood, are marginalized over analytically, with their posteriors later recovered from the chains *a posteriori*.

The MCMC chains are run using the `Montepython` sampler [69, 70]. The plots and marginalized constraints are generated with the `getdist` package [71]. [3]

III. RESULTS

In this section, we present our results. We perform the analysis with both catalogs of massive and light halos.

A. Massive halos

1. $P^{\rm H}$ analysis

We begin by analyzing the auto-power spectrum of most massive halos.

Fig. 1 shows 1D and 2D marginalized posterior distributions for the bias parameters in the 1-loop EFT model. The results are presented for four different $k_{\rm max}$ values: 0.8, 1, 1.5, and $2\,h{\rm Mpc}^{-1}$. We see that the posteriors are consistent with each other. As a frequentest confirmation of our results, we found an equally good fit across all configurations. Starting from $k_{\rm max} = 1.5\,h{\rm Mpc}^{-1}$, we observe that the mean value of $b_2^{\rm H}$ is shifted lower. For $k_{\rm max} = 2\,h{\rm Mpc}^{-1}$, the errors decrease further, and $b_2^{\rm H}$ is lower than zero by 2σ. These $b_2^{\rm H}$ values appear to be in conflict with the halo bias prediction based on the background-split argument from [72], $\tilde{b}_2^{\rm H} = 1.9$ [4]. The observed shifts indicate a mild systematic bias for

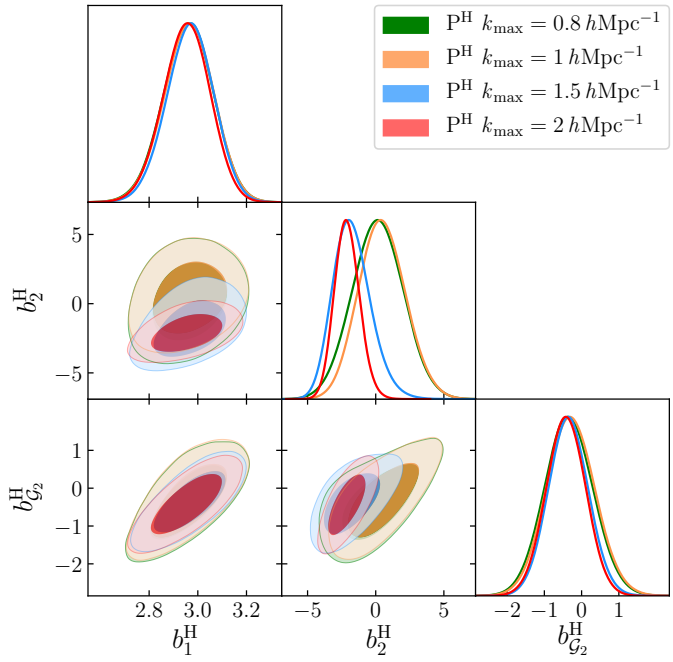

FIG. 1. Marginalized posteriors obtained from the halo power spectrum (massive halos) for different values of $k_{\rm max}$: 0.8, 1, 1.5 and $2\,h{\rm Mpc}^{-1}$ (green, orange, blue, red, respectively).

$k_{\rm max} > 1\,h{\rm Mpc}^{-1}$, likely due to higher-order corrections not accounted for in our one-loop model.

To determine a baseline $k_{\rm max}$ configuration, we quantify the magnitude of the one-loop correction as a function of wavenumber. In Fig. 2, we plot the one-loop contribution divided by the tree-level model. We see that the magnitude of perturbative correction exceeds the linear theory prediction already at $k_{\rm max} = 0.8\,h{\rm Mpc}^{-1}$ for $\mu \gtrsim 0.6$, suggesting that higher-loop corrections may not

[3] https://getdist.readthedocs.io/en/latest/

[4] To estimate $\tilde{b}_2^{\rm H}$, we used the best-fit values of $b_1^{\rm H}$ and $b_{\mathcal{G}_2}^{\rm H}$ from the baseline 3-spectra analysis, as described in Sec. III A 2. Note that in our convention $b_2 = b_2^{\rm ref} + \frac{4}{3} b_{\mathcal{G}_2}$, where $b_2^{\rm ref}$ is the value used in ref. [72].

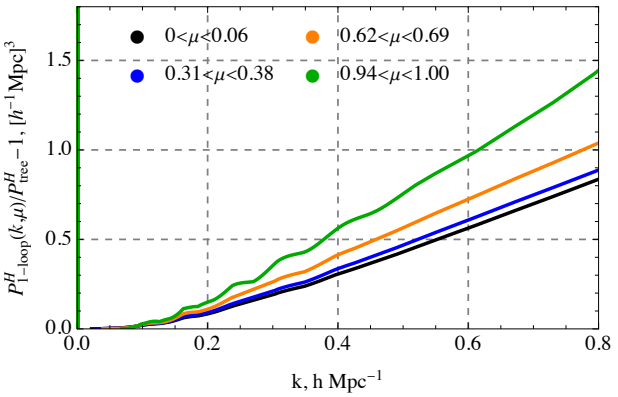

FIG. 2. The magnitude of one-loop corrections relative to the linear theory prediction for massive halos. The theory prediction is based on the best-fit model with $k_{\rm max} = 0.8\,h{\rm Mpc}^{-1}$.

be negligible. [5] Notably, the impact of the one-loop correction increases towards $\mu = 1$. This suggests that the velocity field is primarily responsible for the breakdown of perturbation theory at small scales. Indeed, the velocity field is more nonlinear than the density field for dark matter halos. Strictly speaking, the 1-loop EFT is valid until $k_{\rm max} \simeq 0.6\,h{\rm Mpc}^{-1}$ for the transverse ($\mu \sim 0$) modes and until $k_{\rm max} \simeq 0.4\,h{\rm Mpc}^{-1}$ for the modes along the line of sight ($\mu \sim 1$). Given that no biases are observed at the level of the parameter estimation, it is likely that the two-loop corrections were partly absorbed by the one-loop nuisance parameters and counterterms. We however note that the EFT model can be still applied on these scales as a phenomenological model that is capable to describe the data with high accuracy. Thus, we select $k_{\rm max} = 0.8\,h{\rm Mpc}^{-1}$ as a baseline for the $P^{\rm H}$ analysis.

2. $P^{\rm F} + P^{\rm H} + P^{\rm X}$ *analysis: diagonal covariance*

We present the parameter constraints from the combined analysis of the $P^{\rm H}$, $P^{\rm F}$ and $P^{\rm X}$ spectra. We employ the Gaussian covariance matrix, neglecting the off-diagonal terms. For the halo auto-power spectrum, we fix $k^{\rm H}_{\rm max} = 0.8\,h{\rm Mpc}^{-1}$, as validated in the previous section. For the Lyα forest auto-power spectra, we adopt $k^{\rm F}_{\rm max} = 2\,h{\rm Mpc}^{-1}$ which is lower than the $k^{\rm F}_{\rm max} = 3\,h{\rm Mpc}^{-1}$ value used in ref. [37]. We found that the parameter constraints derived from $P^{\rm F}$-only analysis with $k^{\rm F}_{\rm max} = 3\,h{\rm Mpc}^{-1}$ are inconsistent with those obtained from the combined $P^{\rm F} + P^{\rm H} + P^{\rm X}$ analysis. As detailed in App. A, this discrepancy can be attributed to higher-order corrections in the Lyα forest power spectrum, which shift the posteriors to a new minimum. Therefore, we select a more conservative $k^{\rm F}_{\rm max}$ value.

Fig. 3 shows the 1D and 2D marginalized posterior distributions for the bias parameters derived from various data combinations. The results of 3-spectra analyses are presented for four different $k^{\rm X}_{\rm max}$ values: 0.8, 1, 1.5, and $2\,h{\rm Mpc}^{-1}$. We see that the posteriors obtained from the auto-power spectra $P^{\rm F}$ and $P^{\rm H}$ are fully consistent with those from the $P^{\rm F} + P^{\rm H} + P^{\rm X}$ analysis up to $k^{\rm X}_{\rm max} = 1.5\,h{\rm Mpc}^{-1}$. For $k^{\rm X}_{\rm max} = 2\,h{\rm Mpc}^{-1}$, the contours for the linear biases b_1 and b_η are significantly shifted compared to the results with lower $k^{\rm X}_{\rm max}$ values. These shifts suggest that the fit is biased for $k^{\rm X}_{\rm max} = 2\,h{\rm Mpc}^{-1}$.

As a validation of our scale cuts, we perform a χ^2 test for the $P^{\rm F}+P^{\rm H}+P^{\rm X}$ analysis. For $k^{\rm X}_{\rm max} = 1\,h{\rm Mpc}^{-1}$, the nominal χ^2 statistics across the 355 data points is 372. This indicates a satisfactory fit for 27 free parameters. It is important to note, however, our EFT parameters are quite degenerate and hence the counting of degrees of freedom is not straightforward. [6] The fit quality rapidly deteriorates at higher $k^{\rm X}_{\rm max}$ values: for $k^{\rm X}_{\rm max} = 1.5$, the χ^2 values increase to 404 for 371 data points; for $k^{\rm X}_{\rm max} = 2$ it rises to 506 for 387 data points. These results suggest to choose $k^{\rm X}_{\rm max} = 1\,h{\rm Mpc}^{-1}$ as a baseline.

Tab. I presents the 1D marginalized parameter constraints for the baseline analyses. First, we see that the $P^{\rm F}$-only analysis provides the informative constraints on all Lyman alpha bias parameters within their priors. This validates our choice of EFT priors and showcases the power of the EFT approach. Although the leading-order counterterms for Lyα forest are of order 10^{-2}, c_2 and c_4 are detected with high significance that motivates their inclusion in the analysis. Second important observation is that the inclusion of $P^{\rm X}$ significantly improves the constraints obtained from the individual auto-power spectra. In particular, the errors on Lyα forest non-linear bias parameters b_2, $b_{\mathcal{G}_2}$, b_{η^2}, $b_{\delta\eta}$, $b_{\Pi^{[2]}_\parallel}$ are reduced by more than a factor of 2, while for $b_{(KK)_\parallel}$ the improvement exceeds a factor of 4 relative to the $P^{\rm F}$-only analysis. Surprisingly, the uncertainties on the cubic bias parameters and counterterms for Lyα forest remain largely unchanged.

[5] On the practical side, it might be more optimal to employ a μ-dependent $k_{\rm max}$ cutoff. We plan to explore this option in future.

[6] For example, we found that adding the b_{Γ_3} does not affect the quality of the fit.

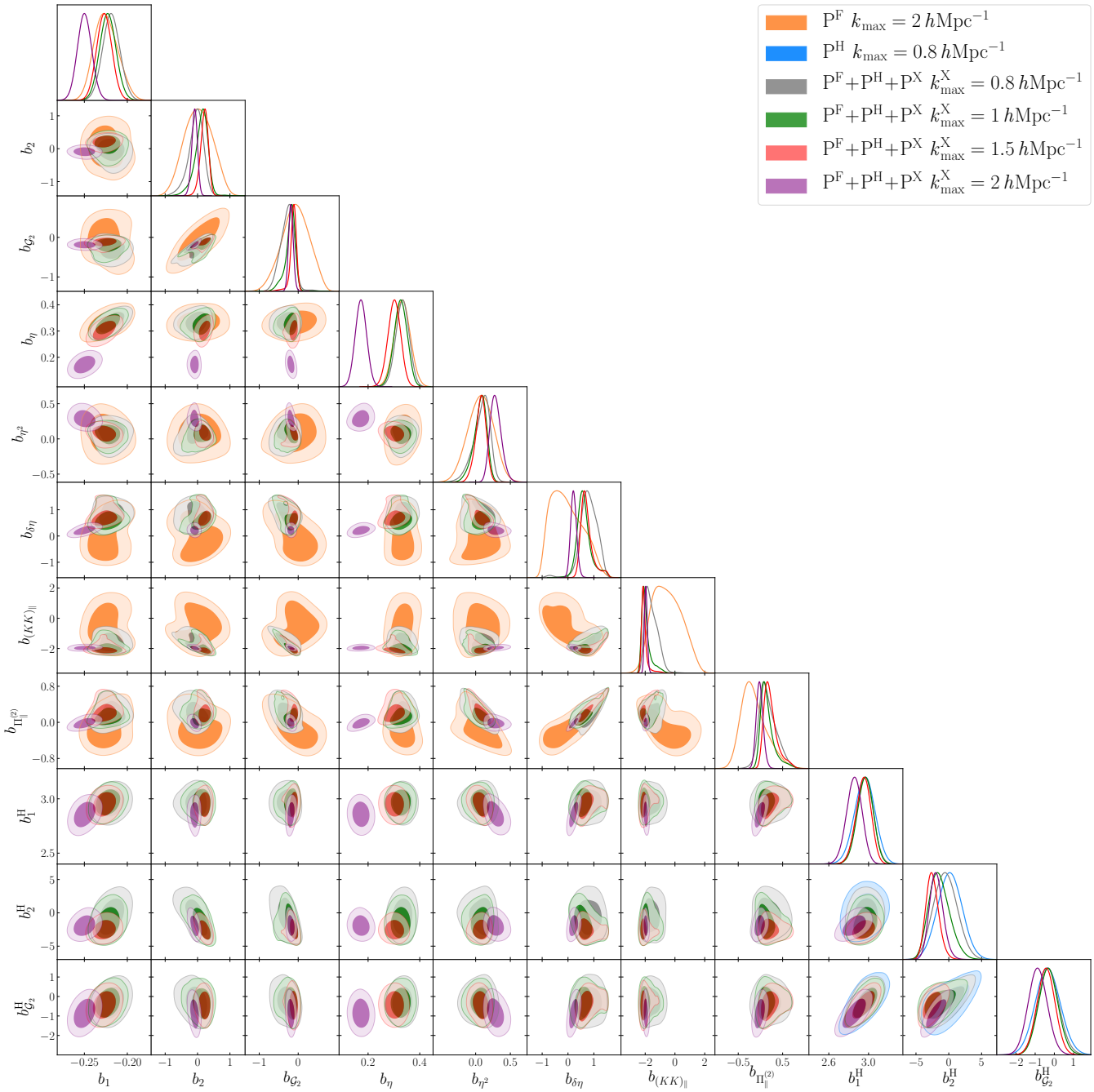

FIG. 3. Marginalized posteriors on nuisance parameters of the EFT model for the Lyα forest auto-power spectrum $P^{\rm F}$ (orange), the massive halo auto-power spectrum $P^{\rm H}$ (blue), and their combination with the Lyα – halo cross-power spectrum $P^{\rm X}$ at $z = 2.8$. The combined analysis results are shown for four different values of $k^{\rm X}_{\rm max}$: 0.8, 1, 1.5, and 2 hMpc^{-1} (gray, green, red, purple, respectively). All results are obtained with the diagonal covariance.

The improvement for the halo bias parameters is more modest, with the most significant impact on $b^{\rm H}_{\Gamma_3}$, whose error is reduced by a factor of 2. At the same time, the halo counterterms and constant shot-noise parameter constraints improve dramatically, ranging from 3 to 23 times better than in the $P^{\rm H}$-only analysis. We conclude that the $P^{\rm F}$, $P^{\rm H}$, and $P^{\rm X}$ probes are highly complementary, and their combination yields a significant information gain.

The best-fit predictions for our baseline 3-spectra model across four angular bins are compared to the data in Fig. 4. The EFT model predicts the $P^{\rm F}$, $P^{\rm H}$ and

Param. \ Data	$P^{\rm F}$	$P^{\rm H}$	$P^{\rm F}+P^{\rm H}+P^{\rm X}$	
			diag cov	off-diag cov
b_1	$-0.2245^{+0.0126}_{-0.0154}$	–	$-0.2226^{+0.0094}_{-0.0098}$	$-0.2184^{+0.0095}_{-0.0098}$
b_η	$0.332^{-0.031}_{-0.031}$	–	$0.326^{+0.026}_{-0.025}$	$0.331^{+0.021}_{-0.020}$
b_2	$0.03^{+0.44}_{-0.46}$	–	$0.11^{+0.24}_{-0.16}$	$0.02^{+0.14}_{-0.12}$
$b_{\mathcal{G}_2}$	$-0.07^{+0.38}_{-0.34}$	–	$-0.21^{+0.16}_{-0.09}$	$-0.28^{+0.18}_{-0.11}$
b_{η^2}	$0.072^{+0.194}_{-0.180}$	–	$0.063^{+0.110}_{-0.075}$	$0.169^{+0.077}_{-0.060}$
$b_{\delta\eta}$	$-0.03^{+0.42}_{-0.83}$	–	$0.63^{+0.18}_{-0.30}$	$0.68^{+0.13}_{-0.25}$
$b_{(KK)_\parallel}$	$-0.51^{+0.86}_{-1.18}$	–	$-1.94^{+0.12}_{-0.36}$	$-1.66^{+0.16}_{-0.41}$
$b_{\Pi^{[2]}_\parallel}$	$-0.142^{+0.212}_{-0.350}$	–	$0.157^{+0.080}_{-0.183}$	$0.023^{+0.052}_{-0.122}$
b_{Γ_3}	$-0.49^{+0.13}_{-0.13}$	–	$-0.07^{+0.12}_{-0.12}$	$0.20^{+0.12}_{-0.12}$
$10^2 c_0/[h^{-1}\mathrm{Mpc}]^2$	$-2.32^{+1.06}_{-1.06}$	–	$-2.73^{+1.07}_{-1.07}$	$-2.74^{+1.05}_{-1.05}$
$10^2 c_2/[h^{-1}\mathrm{Mpc}]^2$	$4.26^{+1.54}_{-1.54}$	–	$5.18^{+1.55}_{-1.55}$	$5.48^{+1.52}_{-1.52}$
$10^2 c_4/[h^{-1}\mathrm{Mpc}]^2$	$-5.38^{+1.0}_{-1.0}$	–	$-7.47^{+1.03}_{-1.03}$	$-7.79^{+1.03}_{-1.03}$
$b_{\Pi^{[3]}_\parallel}$	$0.771^{+0.089}_{-0.089}$	–	$2.085^{+0.088}_{-0.088}$	$2.178^{+0.089}_{-0.089}$
$b_{\delta\Pi^{[2]}_\parallel}$	$-0.05^{+0.19}_{-0.19}$	–	$-0.01^{+0.19}_{-0.19}$	$-0.15^{+0.20}_{-0.20}$
$b_{(K\Pi^{[2]})_\parallel}$	$-1.64^{+0.25}_{-0.25}$	–	$0.66^{+0.25}_{-0.25}$	$-0.33^{+0.25}_{-0.25}$
$b_{\eta\Pi^{[2]}_\parallel}$	$-0.24^{+0.43}_{-0.43}$	–	$-0.17^{+0.43}_{-0.43}$	$-0.16^{+0.44}_{-0.44}$
$b_1^{\rm H}$	–	$2.960^{+0.108}_{-0.102}$	$2.967^{+0.083}_{-0.077}$	$2.804^{+0.087}_{-0.083}$
$b_2^{\rm H}$	–	$0.16^{+1.91}_{-1.92}$	$-1.41^{+1.35}_{-1.80}$	$-1.67^{+1.25}_{-1.36}$
$b_{\mathcal{G}_2}^{\rm H}$	–	$-0.34^{+0.66}_{-0.68}$	$-0.31^{+0.51}_{-0.52}$	$-1.03^{+0.49}_{-0.49}$
$b_{\Gamma_3}^{\rm H}$	–	$-0.03^{+0.53}_{-0.53}$	$-0.71^{+0.25}_{-0.25}$	$-0.05^{+0.36}_{-0.36}$
$c_0^{\rm H}/[h^{-1}\mathrm{Mpc}]^2$	–	$-0.44^{+2.94}_{-2.94}$	$-0.70^{+0.13}_{-0.13}$	$-0.27^{+0.24}_{-0.24}$
$c_2^{\rm H}/[h^{-1}\mathrm{Mpc}]^2$	–	$2.06^{+1.11}_{-1.11}$	$1.73^{+0.23}_{-0.23}$	$1.82^{+0.41}_{-0.41}$
$c_4^{\rm H}/[h^{-1}\mathrm{Mpc}]^2$	–	$3.70^{+1.33}_{-1.33}$	–	–
$\tilde{c}^{\rm H}/[h^{-1}\mathrm{Mpc}]^4$	–	$-1.67^{+1.42}_{-1.42}$	$2.31^{+0.49}_{-0.49}$	$2.37^{+0.71}_{-0.71}$
$P^{\rm H}_{\rm shot}$	–	$-0.066^{+0.764}_{-0.764}$	$0.101^{+0.054}_{-0.054}$	$0.035^{+0.037}_{-0.037}$
$a_0^{\rm H}$	–	$0.04^{+0.97}_{-0.97}$	$-0.16^{+0.89}_{-0.89}$	$0.10^{+0.73}_{-0.73}$
$a_2^{\rm H}$	–	$-0.03^{+1.0}_{-1.0}$	$0.19^{+0.97}_{-0.97}$	$0.52^{+0.93}_{-0.93}$
$\tilde{c}^{\rm X}/[h^{-1}\mathrm{Mpc}]^4$	–	–	$0.238^{+0.086}_{-0.086}$	$1.252^{+0.317}_{-0.317}$

TABLE I. One-dimensional marginalized constraints on nuisance parameters of the one-loop EFT model from the Lyα forest auto-power spectrum with $k^{\rm F}_{\rm max} = 2\ h\mathrm{Mpc}^{-1}$ (second column), the massive halo auto-power spectrum with $k^{\rm H}_{\rm max} = 0.8\ h\mathrm{Mpc}^{-1}$ (third column) and their combination with the Lyα – halo cross-power spectrum with $k^{\rm X}_{\rm max} = 1\ h\mathrm{Mpc}^{-1}$, using diagonal covariance (fourth column) and with $k^{\rm X}_{\rm max} = 0.8\ h\mathrm{Mpc}^{-1}$ using off-diagonal covariance (fifth column) at $z = 2.8$. Parameter constraints related to each respective spectrum are grouped together. The parameters in the upper section were directly sampled in our MCMC chains, while the parameters in the lower section were analytically marginalized in the likelihood, with their posteriors recovered from the chains *a posteriori*.

$P^{\rm X}$ data at $(k^{\rm F}_{\rm max}, k^{\rm H}_{\rm max}, k^{\rm X}_{\rm max}) = (2, 0.8, 1)\, h\mathrm{Mpc}^{-1}$ with the nominal 0.9%, 3.9% and 0.8% accuracy, respectively. The residuals grow at lower k due to the significant cosmic variance of the Sherwood simulation. These results represent a significant improvement over the previous analysis [43], which described the Lyα – halo cross-power spectrum data with a 10% error up to scales of $k^{\rm X}_{\rm max} = 1\, h\mathrm{Mpc}^{-1}$.

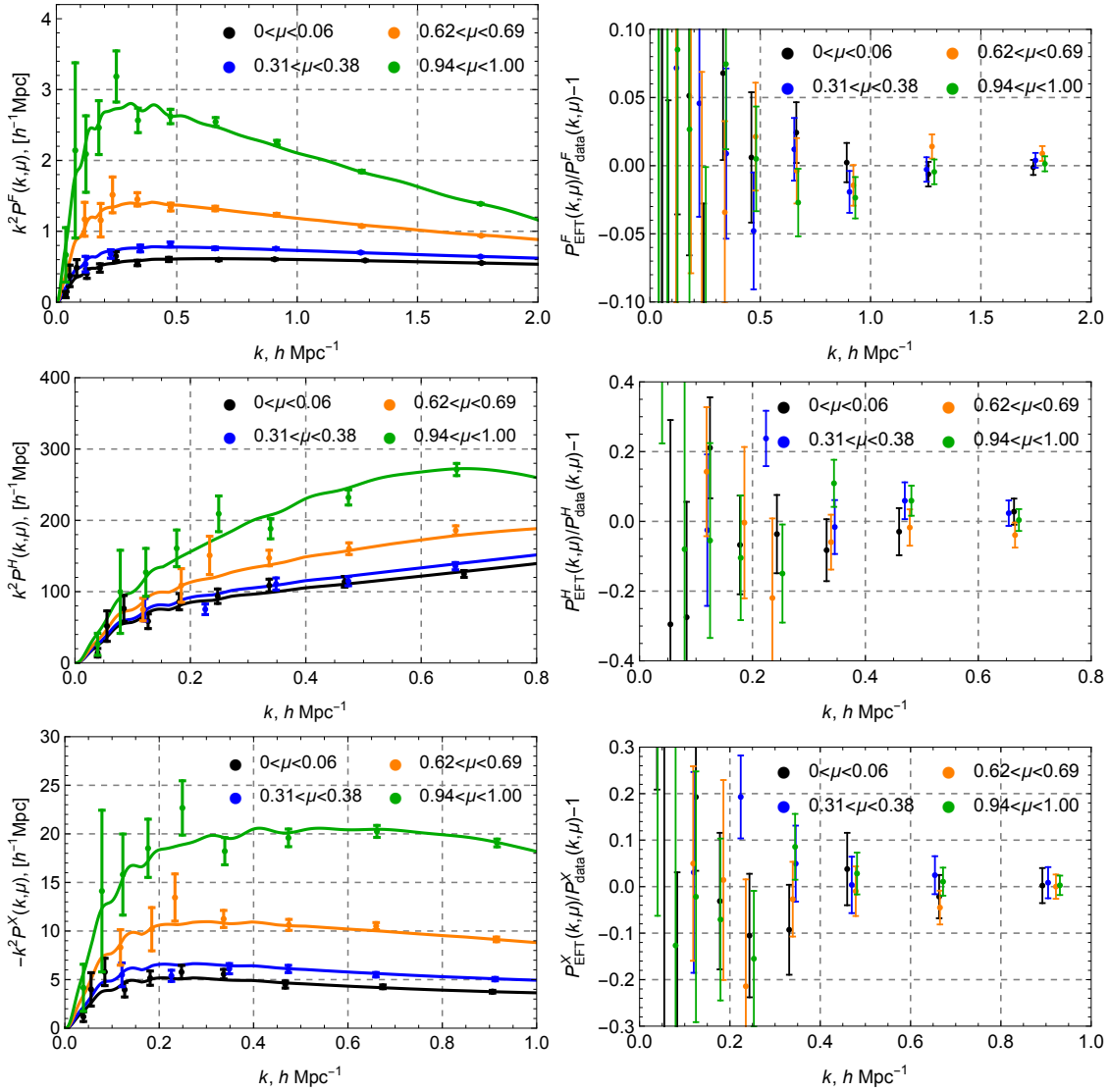

FIG. 4. Best-fit EFT predictions against the simulated power spectra (left panel), and the residuals between the model and the data (right panel). The best-fit model was obtained in the 3-spectra analysis for the most massive halos with $(k^{\rm F}_{\rm max}, k^{\rm H}_{\rm max}, k^{\rm X}_{\rm max}) = (2, 0.8, 1)\,h{\rm Mpc}^{-1}$. The constant shot-noise contribution is subtracted from the $P^{\rm H}$ data.

3. $P^{\rm F} + P^{\rm H} + P^{\rm X}$ *analysis: off-diagonal covariance*

We now present the results of the 3-spectra analysis using the full off-diagonal covariance (4), (5).

Fig. 5 shows the 1D and 2D marginalized posterior distributions for the bias parameters derived from various data combinations. The results are shown for five different $k^{\rm X}_{\rm max}$ values: 0.4, 0.8, 1, 1.5, and $2\,h{\rm Mpc}^{-1}$. We observe that the constraints obtained from the $P^{\rm F}$ and $P^{\rm LH}$ individually remain consistent with those from the combined 3-spectra analysis up to $k^{\rm X}_{\rm max} = 1.5\,h{\rm Mpc}^{-1}$. However, the posteriors shift more rapidly as $k^{\rm X}_{\rm max}$ increases compared to analysis with the diagonal covariance, cf. with Fig. 3. This indicates that the off-diagonal terms in the covariance introduce additional constraints, leading to a worse fit. Specifically, for $k^{\rm X}_{\rm max} = 0.4\,h{\rm Mpc}^{-1}$, the minimum χ^2 value is 401 for 307 data points, while for $k^{\rm X}_{\rm max} = 0.8\,h{\rm Mpc}^{-1}$, it is 436 for 339 data points. With 27 free parameters, these results indicate similarly poor fits for both configurations. Given that the best-fit χ^2 statistics deteriorate rapidly for $k^{\rm X}_{\rm max} > 0.8\,h{\rm Mpc}^{-1}$ and the posteriors remain consistent at smaller scale cuts, we choose $k^{\rm X}_{\rm max} = 0.8\,h{\rm Mpc}^{-1}$ as a baseline for the 3-spectra analysis with off-diagonal covariance.

Tab. I compares the constraints on EFT parameters obtained when using the diagonal covariance (fifth col-

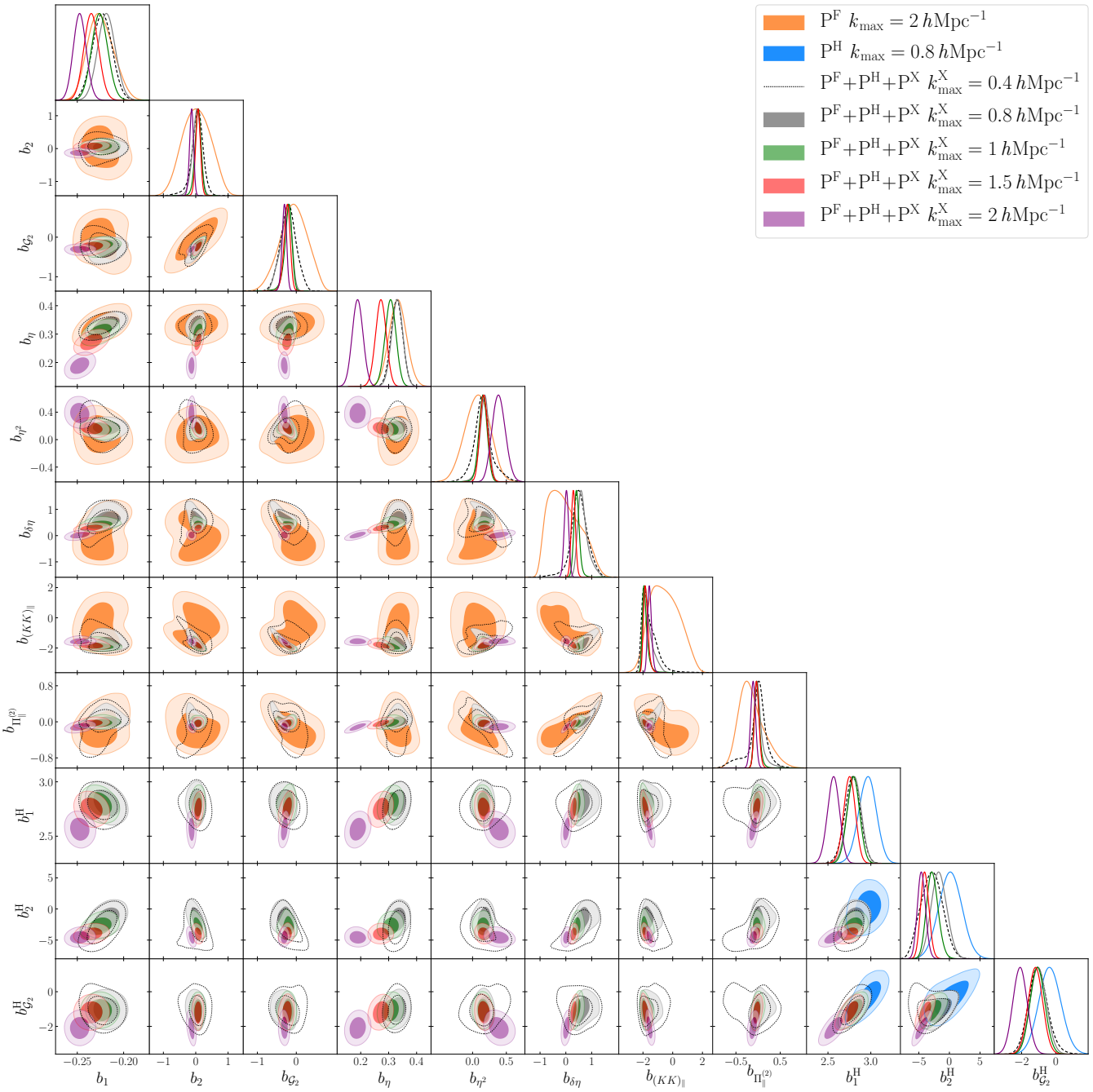

FIG. 5. Marginalized posteriors on nuisance parameters of the EFT model for the Lyα forest auto-power spectrum $P^{\rm F}$ (orange), the massive halo auto-power spectrum $P^{\rm H}$ (blue), and their combination with the Lyα – halo cross-power spectrum $P^{\rm X}$ at $z = 2.8$. The combined analysis results are shown for four different values of $k^{\rm X}_{\rm max}$: 0.4, 0.8, 1, 1.5, and 2 hMpc^{-1} (dashed black, gray, green, red, purple, respectively). All results are obtained with the off-diagonal covariance.

umn) and the off-diagonal covariance (forth column). For Lyα forest parameters and halo stochasticity parameters, the analysis with the off-diagonal covariance yields tighter constraints than the analysis with diagonal covariance. As discussed earlier, this improvement stem from off-diagonal terms in the covariance, which introduce additional correlations between data points. At the same time, the halo counterterms are better constrained in the analysis with the diagonal covariance, which can be explained by the higher value $k^{\rm X}_{\rm max} = 1\,h$Mpc^{-1}used there. Overall, the constraints from the baseline analyses with diagonal and off-diagonal covariances are consistent

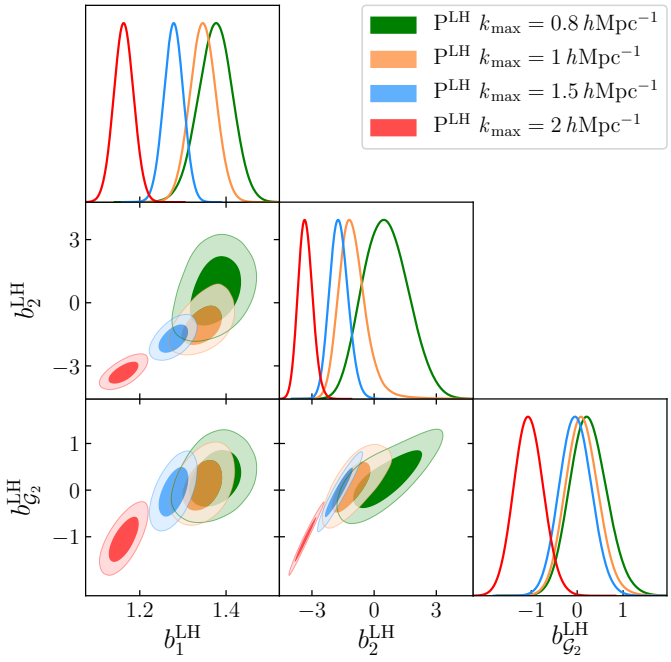

FIG. 6. Marginalized posteriors obtained from the $P^{\rm LH}$ for different values of $k_{\rm max}$: 0.8, 1, 1.5 and $2\,h$Mpc^{-1} (green, orange, blue, red, respectively).

with each other. This validates our analysis procedure, including the adopted data cuts.

B. All halos

1. $P^{\rm LH}$ *analysis*

In this section, we present the results obtained from the complete halo catalog. We start with the analysis of the auto-power spectrum of light halos.

Fig. 6 shows the posterior distributions for the bias parameters. The constraints on the bias parameters appear to be tighter compared to those from the $P^{\rm H}$ analysis, cf. with Fig. 1. This improvement can be attributed to the higher number density of the full halo catalog. Consequently, as $k_{\rm max}$ increases, the contours shifts more rapidly, implying that the perturbative approach for light halos breaks down at smaller scales. For $k_{\rm max} = 1\,h$Mpc^{-1}, the best-fit χ^2 statistics shows a good agreement with the data. However, for smaller data cuts, the fit quality deteriorates substantially, leading to shifts in the posteriors. For instance, for $k_{\rm max} = 2\,h$Mpc^{-1}, the parameter $b_2^{\rm LH} = -3.3 \pm 0.4$ shows a significant tension with the peak-background split result $\tilde{b}_2^{\rm LH} = -0.6$ [72] and the measurements of [73], suggesting a biased fit. [7]

We evaluate the magnitude of the one-loop correction. Our analysis shows that one-loop contribution remains below 20% of the linear theory prediction up to scales of $k_{\rm max} = 0.8\,h$Mpc^{-1}. Thus, we select a conservative scale cut $k_{\rm max} = 0.8\,h$Mpc^{-1} as a baseline for the all-halo power spectrum analysis. This choice also justifies the scale cut used in the $P^{\rm H}$ analysis in Sec. III A, as the full halo catalog, with its greater statistical power, offers a more stringent test of the theoretical model. Additionally, using the same scale cut $k_{\rm max}$ for both the light and most massive halos facilitates a direct comparison of the results.

2. $P^{\rm F} + P^{\rm LH} + P^{\rm X}$ *analysis: diagonal covariance*

We now present the parameter constraints from the combined $P^{\rm F} + P^{\rm LH} + P^{\rm X}$ analysis. Consistent with the analysis of the most massive halos, we fix $k^{\rm F}_{\rm max} = 2\,h$Mpc^{-1} and $k^{\rm H}_{\rm max} = 0.8\,h$Mpc^{-1}, and vary $k^{\rm X}_{\rm max}$ independently.

Fig. 7 shows the 1D and 2D marginalized posterior distributions for the bias parameters derived from various data combinations. The constraints derived from $P^{\rm F}$ and $P^{\rm LH}$ individually are entirely consistent with those from the 3-spectra analysis up to $k^{\rm X}_{\rm max} = 1\,h$Mpc^{-1}. The largest difference is observed in the b_2 parameter, whose posterior remains consistent between the two analyses at the 2σ level. For $k^{\rm X}_{\rm max} > 1\,h$Mpc^{-1}, the contours for the linear bias parameter b_η shift progressively. This suggests that the fit is biased already at $k^{\rm X}_{\rm max} = 1\,h$Mpc^{-1}.

To confirm our scale cuts, we perform a χ^2 test for the combined 3-spectra analysis. For $k^{\rm X}_{\rm max} = 0.8\,h$Mpc^{-1}, the best-fit χ^2 statistic is 372 across the 339 data points, indicating a satisfactory fit for 27 free parameters. For $k^{\rm X}_{\rm max} = 1\,h$Mpc^{-1}, the χ^2 value increases to 402 for the 355 data points. For $k^{\rm X}_{\rm max} > 1\,h$Mpc^{-1}, the fit quality deteriorates rapidly. Given that the fit quality for $k^{\rm X}_{\rm max} = 0.8\,h$Mpc^{-1} and $k^{\rm X}_{\rm max} = 1\,h$Mpc^{-1} is comparable and that their posteriors are consistent, we adopt $k^{\rm X}_{\rm max} = 1\,h$Mpc^{-1} as our baseline scale cut. In Appendix B, we demonstrate that the fit to the 3-spectra for light halos can be significantly improved by introducing one additional phenomenological free parameter.

[7] See footnote 4.

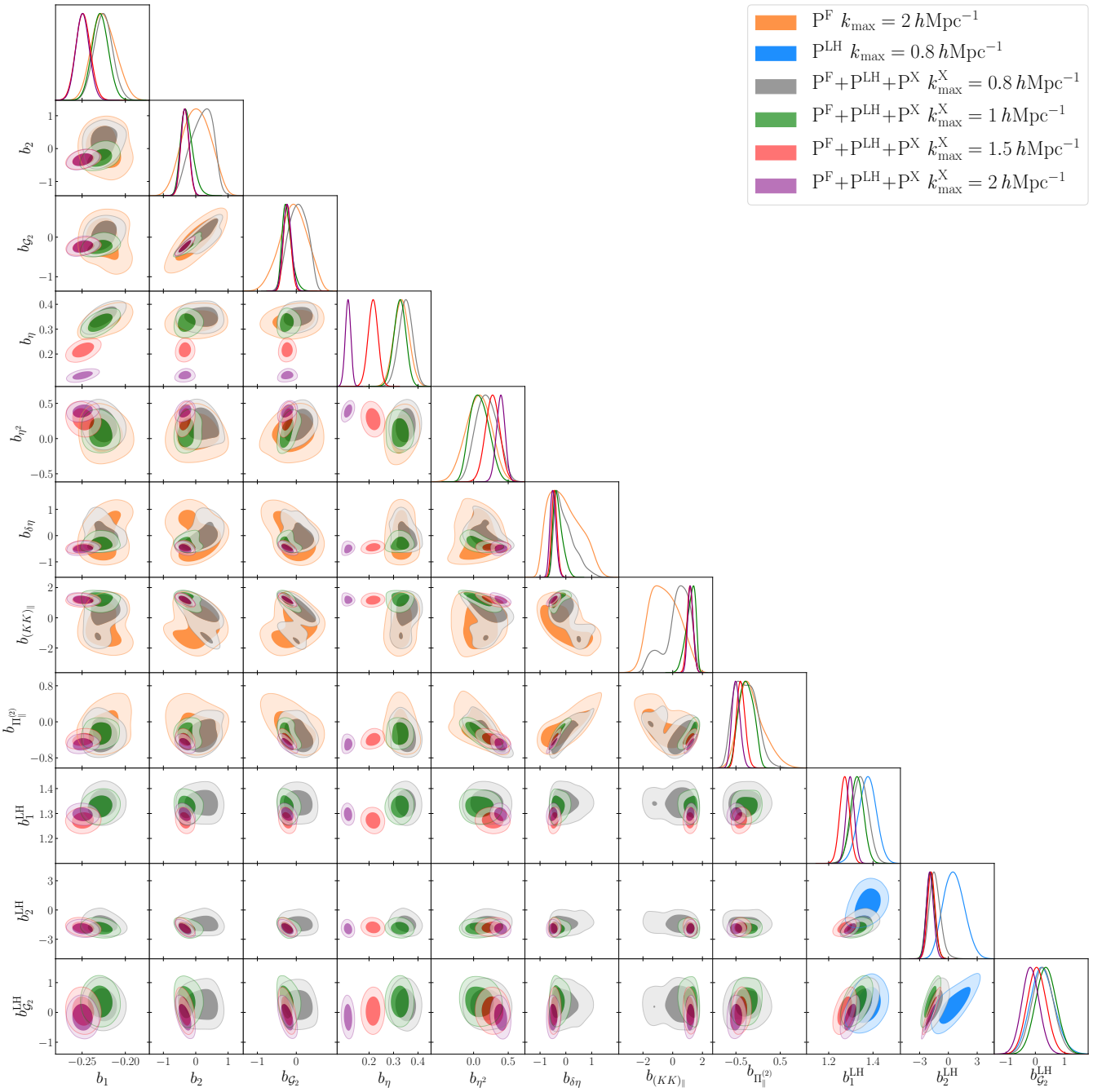

FIG. 7. Marginalized posteriors on nuisance parameters of the EFT model for the Lyα forest auto-power spectrum $P^{\rm F}$ (orange), the all-halo auto-power spectrum $P^{\rm LH}$ (blue), and their combination with the Lyα – all-halo cross-power spectrum $P^{\rm X}$ at $z = 2.8$. The combined analysis results are shown for four different values of $k^{\rm X}_{\rm max}$: 0.8, 1, 1.5, and 2 hMpc^{-1} (gray, green, red, purple, respectively). The results are obtained with the diagonal covariance.

The 1D marginalized parameter constraints for the baseline configurations are given in Tab. II. The inclusion of $P^{\rm X}$ significantly improve the constraints obtained from the $P^{\rm F}$ and $P^{\rm LH}$ individually. For the Lyman-α forest bias parameters, the errors are reduced by factors ranging from 1.3 to 3.6 compared to the $P^{\rm F}$-only analysis. Interestingly, unlike the analysis of the most massive halos, the constraints on the Lyman-α forest counterterms improve relative to the $P^{\rm F}$-only analysis; for instance, the uncertainty on c_0 is reduced by a factor of 1.6. For the halo bias parameters, the improvement is similar to the analysis in Sec. III A 2, with the most significant impact

Param. \ Data	$P^{\rm F}$	$P^{\rm LH}$	$P^{\rm F}+P^{\rm LH}+P^{\rm X}$	
			diag cov	off-diag cov
b_1	$-0.2245^{+0.0126}_{-0.0154}$	–	$-0.2291^{+0.0095}_{-0.0098}$	$-0.2125^{+0.0084}_{-0.0087}$
b_η	$0.332^{-0.031}_{-0.031}$	–	$0.326^{+0.026}_{-0.024}$	$0.346^{+0.016}_{-0.015}$
b_2	$0.03^{+0.44}_{-0.46}$	–	$-0.27^{+0.15}_{-0.22}$	$0.61^{+0.10}_{-0.07}$
$b_{\mathcal{G}_2}$	$-0.07^{+0.38}_{-0.34}$	–	$-0.24^{+0.09}_{-0.15}$	$0.40^{+0.07}_{-0.05}$
b_{η^2}	$0.072^{+0.194}_{-0.180}$	–	$-0.087^{+0.126}_{-0.154}$	$0.191^{+0.084}_{-0.077}$
$b_{\delta\eta}$	$-0.03^{+0.42}_{-0.83}$	–	$-0.30^{+0.13}_{-0.22}$	$-0.16^{+0.09}_{-0.16}$
$b_{(KK)_\parallel}$	$-0.51^{+0.86}_{-1.18}$	–	$1.20^{+0.41}_{-0.23}$	$0.11^{+0.08}_{-0.14}$
$b_{\Pi^{[2]}_\parallel}$	$-0.142^{+0.212}_{-0.350}$	–	$-0.266^{+0.166}_{-0.175}$	$-0.353^{+0.069}_{-0.117}$
b_{Γ_3}	$-0.49^{+0.13}_{-0.13}$	–	$-0.32^{+0.11}_{-0.11}$	$-1.69^{+0.11}_{-0.11}$
$10^2 c_0/[h^{-1}\mathrm{Mpc}]^2$	$-2.32^{+1.06}_{-1.06}$	–	$-2.66^{+0.65}_{-0.65}$	$-2.36^{+0.48}_{-0.48}$
$10^2 c_2/[h^{-1}\mathrm{Mpc}]^2$	$4.26^{+1.54}_{-1.54}$	–	$3.50^{+1.20}_{-1.20}$	$5.04^{+1.07}_{-1.07}$
$10^2 c_4/[h^{-1}\mathrm{Mpc}]^2$	$-5.38^{+1.0}_{-1.0}$	–	$-3.03^{+0.90}_{-0.90}$	$-6.04^{+0.90}_{-0.90}$
$b_{\Pi^{[3]}_\parallel}$	$0.771^{+0.089}_{-0.089}$	–	$0.931^{+0.085}_{-0.085}$	$1.163^{+0.079}_{-0.079}$
$b_{\delta\Pi^{[2]}_\parallel}$	$-0.05^{+0.19}_{-0.19}$	–	$-0.17^{+0.18}_{-0.18}$	$-0.56^{+0.19}_{-0.19}$
$b_{(K\Pi^{[2]})_\parallel}$	$-1.64^{+0.25}_{-0.25}$	–	$-3.07^{+0.20}_{-0.20}$	$-1.81^{+0.22}_{-0.22}$
$b_{\eta\Pi^{[2]}_\parallel}$	$-0.24^{+0.43}_{-0.43}$	–	$0.54^{+0.42}_{-0.42}$	$0.01^{+0.43}_{-0.43}$
$b_1^{\rm LH}$	–	$1.375^{+0.042}_{-0.039}$	$1.327^{+0.030}_{-0.030}$	$1.266^{+0.037}_{-0.035}$
$b_2^{\rm LH}$	–	$0.58^{+1.03}_{-1.20}$	$-1.86^{+0.41}_{-0.46}$	$-2.03^{+0.44}_{-0.50}$
$b_{\mathcal{G}_2}^{\rm LH}$	–	$0.25^{+0.39}_{-0.44}$	$0.37^{+0.37}_{-0.37}$	$0.09^{+0.34}_{-0.36}$
$b_{\Gamma_3}^{\rm LH}$	–	$0.14^{+0.13}_{-0.13}$	$-0.18^{+0.08}_{-0.08}$	$-0.61^{+0.10}_{-0.08}$
$c_0^{\rm LH}/[h^{-1}\mathrm{Mpc}]^2$	–	$0.024^{+0.087}_{-0.087}$	$-0.196^{+0.051}_{-0.051}$	$-0.091^{+0.062}_{-0.062}$
$c_2^{\rm LH}/[h^{-1}\mathrm{Mpc}]^2$	–	$1.404^{+0.159}_{-0.159}$	$-0.240^{+0.065}_{-0.065}$	$-0.323^{+0.087}_{-0.087}$
$c_4^{\rm LH}/[h^{-1}\mathrm{Mpc}]^2$	–	$2.15^{+0.42}_{-0.42}$	–	–
$\tilde{c}^{\rm LH}/[h^{-1}\mathrm{Mpc}]^4$	–	$-0.81^{+0.77}_{-0.77}$	$3.53^{+0.22}_{-0.22}$	$3.93^{+0.20}_{-0.20}$
$P_{\rm shot}^{\rm LH}$	–	$0.001^{+1.0}_{-1.0}$	$-0.24^{+0.95}_{-0.95}$	$-0.08^{+0.84}_{-0.84}$
$a_0^{\rm LH}$	–	$0.0^{+1.0}_{-1.0}$	$0.0^{+1.0}_{-1.0}$	$0.02^{+1.0}_{-1.0}$
$a_2^{\rm LH}$	–	$0.0^{+1.0}_{-1.0}$	$0.0^{+1.0}_{-1.0}$	$0.02^{+1.0}_{-1.0}$
$\tilde{c}^{\rm X}/[h^{-1}\mathrm{Mpc}]^4$	–	–	$0.623^{+0.049}_{-0.049}$	$1.768^{+0.098}_{-0.098}$

TABLE II. One-dimensional marginalized constraints on nuisance parameters of the one-loop EFT model from the Lyα forest auto-power spectrum with $k^{\rm F}_{\rm max} = 2\ h\mathrm{Mpc}^{-1}$ (second column), the all-halo auto-power spectrum with $k^{\rm H}_{\rm max} = 0.8\ h\mathrm{Mpc}^{-1}$ (third column) and their combination with the Lyα – all-halo cross-power spectrum with $k^{\rm X}_{\rm max} = 1\ h\mathrm{Mpc}^{-1}$ using diagonal covariance (fourth column) and with $k^{\rm X}_{\rm max} = 0.8\ h\mathrm{Mpc}^{-1}$ using off-diagonal (fifth column) at $z = 2.8$. Parameter constraints related to each respective spectrum are grouped together. The parameters in the upper section were directly sampled in our MCMC chains, while the parameters in the lower section were analytically marginalized in the likelihood, with their posteriors recovered from the chains *a posteriori*.

on $b_2^{\rm H}$, whose error is decreases by more than a factor of 2. The improvement for the halo counterterms ranges from 1.7 to 3.5 times. We conclude that the $P^{\rm F}$, $P^{\rm LH}$, and $P^{\rm X}$ measurements are highly complementary, though the information gain is somewhat reduced compared to the analysis of the most massive halos. This reduction can be attributed to the greater statistical power of the light halo power spectrum, which diminishes the impact of the

cross-correlation in the 3-spectra analysis.

The best-fit predictions for our baseline 3-spectrum model across four angular bins are shown in Fig. 8. The EFT model describes the $P^{\rm F}$, $P^{\rm LH}$ and $P^{\rm X}$ data at $(k^{\rm F}_{\rm max}, k^{\rm H}_{\rm max}, k^{\rm X}_{\rm max}) = (2, 0.8, 1)\,h{\rm Mpc}^{-1}$ with 0.8%, 3.4% and 1.1% accuracy, respectively. We found a mild improvement in the modeling of the halo auto-power spectrum relative to the analysis in Sec. III A 2. This accuracy can be further enhanced to 2% by including an additional free parameter, as detailed in App.B. Our findings demonstrate a fivefold improvement in modeling the Lyα – halo cross-power spectrum compared to the earlier analysis in ref. [43], which only achieved 5% accuracy up to $k^{\rm X}_{\rm max} = 1\,h{\rm Mpc}^{-1}$ for light halos.

Finally, as an extension of our analysis, we add $P^{\rm X}_{\rm shot}$ to the fit at $k^{\rm X}_{\rm max} = 1\ h{\rm Mpc}^{-1}$. We do not detect this parameter in the data. Our 68% constraint reads

$$\frac{P^{\rm X}_{\rm shot}}{[h^{-1}{\rm Mpc}]^3} = 0.15 \pm 0.19\,.$$

We have additionally checked in post-processing that adding $P^{\rm X}_{\rm shot}$ to the best-fit models from other analyses does not improve the fit and does not increase the accuracy of the EFT model at higher $k_{\rm max}$. These analyses validate our baseline choice $P^{\rm X}_{\rm shot} = 0$.

3. $P^{\rm F} + P^{\rm LH} + P^{\rm X}$ *analysis: off-diagonal covariance*

We now proceed to the 3-spectra analysis with the full off-diagonal covariance.

Fig. 9 shows the 1D and 2D marginalized posterior distributions for the bias parameters derived from various data combinations. Up to $k^{\rm X}_{\rm max} = 0.8\,h{\rm Mpc}^{-1}$, the constraints from the combined 3-spectra analysis remain consistent with those obtained from the $P^{\rm F}$ and $P^{\rm LH}$ individually. The largest difference is seen for the $b_2^{\rm LH}$ parameter, which posteriors deviate at the 2.1σ level – a difference still within nominal statistical consistency. As $k^{\rm X}_{\rm max}$ increases, the posteriors shift more rapidly compared to the analysis with the diagonal matrix, cf. Fig. 7. For $k^{\rm X}_{\rm max} > 0.8\,h{\rm Mpc}^{-1}$, the selection-dependent bias b_η exhibits the most significant shifts, indicating a biased fit at these scales.

As a frequentest confirmation of our scale cuts, we found similar fit quality for $k^{\rm X}_{\rm max} < 0.8\,h{\rm Mpc}^{-1}$, while the goodness-of-fit deteriorate rapidly for $k^{\rm X}_{\rm max} > 0.8\,h{\rm Mpc}^{-1}$. Specifically, for $k^{\rm X}_{\rm max} = 0.8\,h{\rm Mpc}^{-1}$ the minimum χ^2 value is 397 across the 339 data points, whereas for $k^{\rm X}_{\rm max} = 1\,h{\rm Mpc}^{-1}$ it sharply increases to 572 for 355 data points. Given 23 free parameters, this behavior suggests that the perturbative approach breaks down at $k^{\rm X}_{\rm max} = 1\,h{\rm Mpc}^{-1}$. Thus, we select $k^{\rm X}_{\rm max} = 0.8\,h{\rm Mpc}^{-1}$ as a baseline for the 3-spectra analysis with the off-diagonal covariance.

Tab. II compares the constraints on EFT parameters obtained when using diagonal covariance and off-diagonal covariance. When using the off-diagonal covariance the errors on Lyα forest parameters and constant shot-noise decrease compared to the analysis with diagonal covariance. However, the agreement between the two analyses is worse than in the case of the most massive halos, cf. Tab. I. For example, the constraints on b_2 and $b_{\mathcal{G}_2}$ differ at the 4.3σ and 4.6σ levels, respectively. The discrepancy for the next-to-leading counterterm $\tilde{c}^{\rm X}$ is even more significant, reaching 10σ, though this can be attributed to overfitting of the data. This degradation in the fit quality can be explained by the additional correlations between data points introduced by the off-diagonal terms in the covariance. We plan to explore this in future.

IV. CONCLUSIONS

We have presented the one-loop EFT model for the cross spectrum of the Lyα forest and a generic biased tracer of matter. Our work is primarily aimed at the analytic description of the Lyα forest – galaxy and Lyα forest – quasar cross correlations. We have found an excellent agreement between our theoretical model and the Lyα-halo data from the Sherwood hydrodynamical simulation data on quasi-linear scales. Specifically, the 1-loop EFT model provides a percent-level accuracy in fitting these data at $k_{\rm max} \simeq 1\ h{\rm Mpc}^{-1}$. Our model can be readily applied to the cross-correlation data from eBOSS and DESI surveys.

Our analysis suggests several directions for further improvements. From the simulation side, we have only analyzed the friends-of-friends halo catalogs, which underestimate the non-linear redshift-space distortions, known as the fingers-of-God [74]. Thus, it will be important to extend our study to Rockstar [75] and COMPASO [76] halo finders, which captures fingers-of-God more accurately (see e.g. [66, 77] and references therein). In addition, it will be interesting to apply our model to simulated galaxies whose properties are close to the realistic samples.

From the theory point of view, it will be interesting

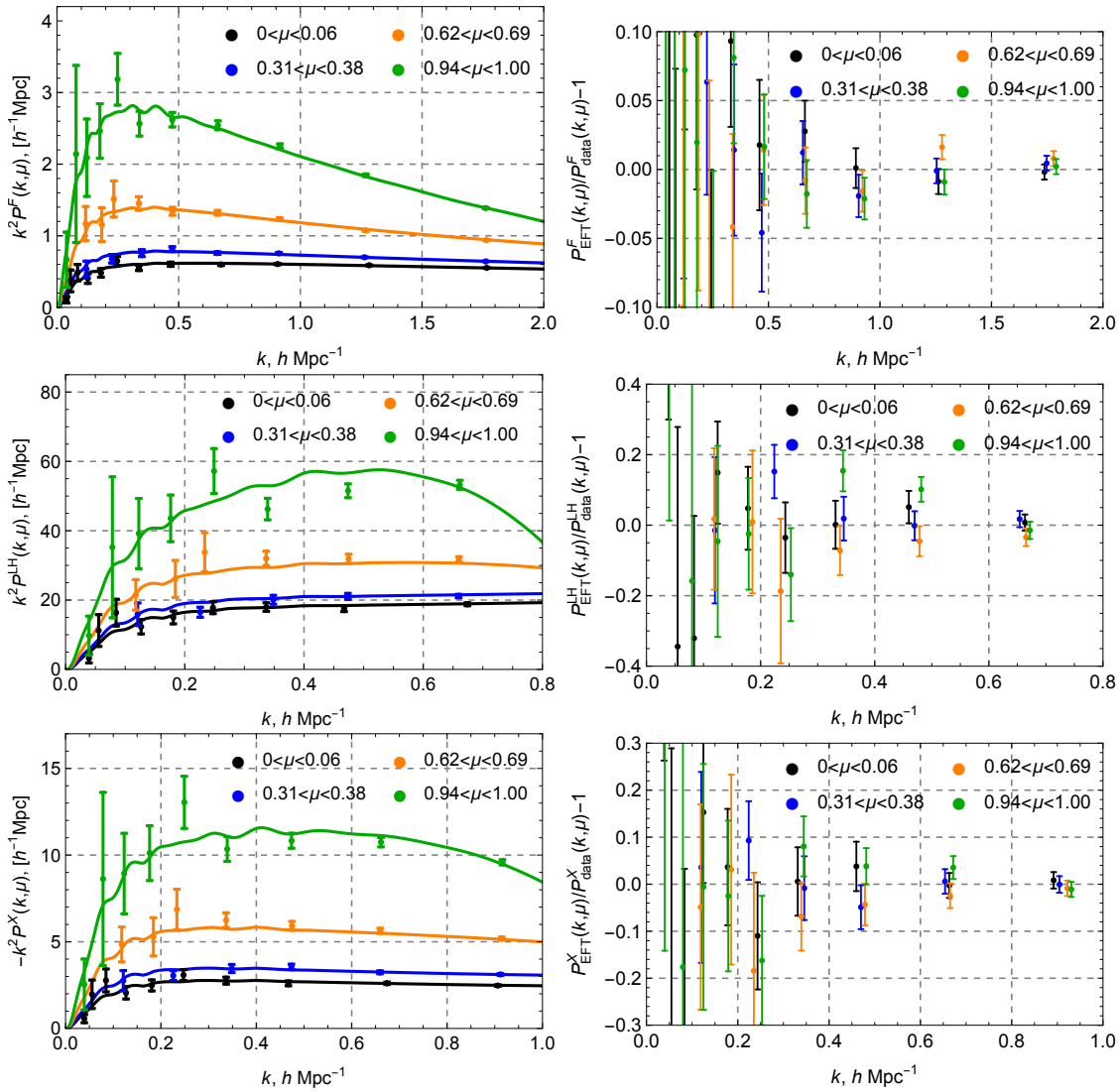

FIG. 8. Best-fit EFT predictions against the simulated power spectra (left panel), and the residuals between the model and the data (right panel). The best-fit model was obtained in the 3-spectra analysis for light halos with $(k^{\rm F}_{\rm max}, k^{\rm H}_{\rm max}, k^{\rm X}_{\rm max}) = (2, 0.8, 1)\,h{\rm Mpc}^{-1}$. The constant shot-noise contribution is subtracted from the $P^{\rm LH}$ data.

to extend our model to higher order statistics, such as the Lyα-galaxy bispectrum. The particular configuration dependencies of higher order statistics will allow one to break degeneracies between EFT parameters and eventually improve cosmological constraints. Moving forward, it will be important to develop simulation based priors for the Lyα forest and high redshift galaxies along the lines of [66, 78].

The ultimate goal of EFT modeling is to infer cosmological parameters from the actual data. For that one has to extend our analysis to cosmological parameters, starting with validations against mock data that resemble the actual observations in terms of clustering properties. The Sherwood data that we used here does not have large enough volume for this purpose, but it can be done with larger simulation suites such as ACCEL2 [79].

Finally, it will be interesting to understand how the Lyα-quasar cross-correlations are affected in the presence of new physics. For instance, it is known that the bispectrum of different tracers can be used to test the equivalence principle [80–85]. As example of such scenario is the violation of Lorentz invariance in the dark matter sector [86, 87]. Since the Lyα forest primarily tracers baryons (which obey the equivalence principle with high precision), while quasars trace dark matter, one could expect the Lyα-quasar bispectrum to be a sensitive probe of

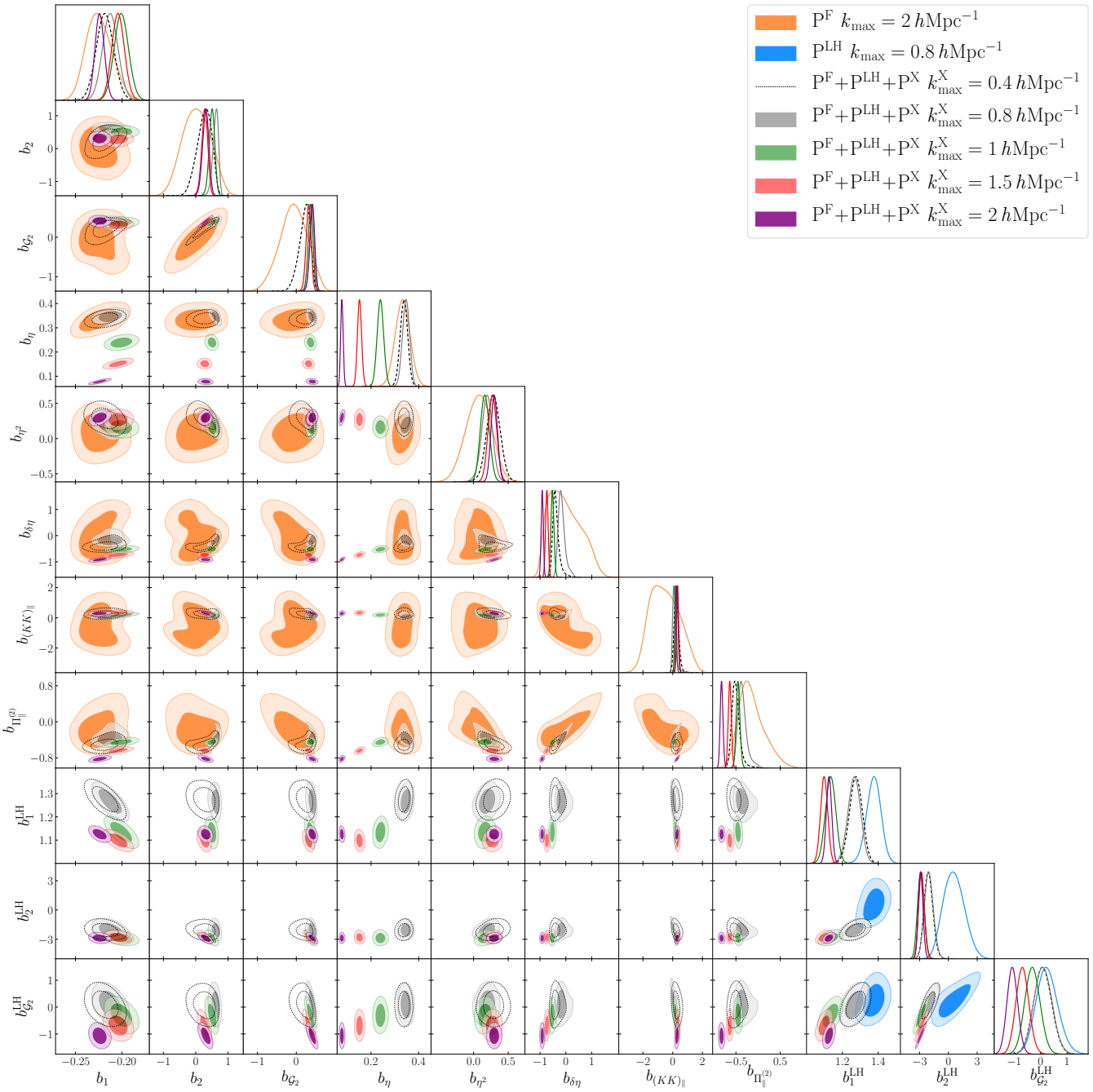

FIG. 9. Marginalized posteriors on nuisance parameters of the EFT model for the Lyα forest auto-power spectrum $P^{\rm F}$ (orange), the all-halo auto-power spectrum $P^{\rm LH}$ (blue), and their combination with the Lyα – all-halo cross-power spectrum $P^{\rm X}$ at $z = 2.8$. The combined analysis results are shown for four different values of $k^{\rm X}_{\rm max}$: 0.4, 0.8, 1, 1.5, and 2 hMpc^{-1} (dashed black, gray, green, red, purple, respectively). The results are obtained with the off-diagonal covariance.

this scenario. We leave this and other research directions listed above for future exploration.

ACKNOWLEDGMENTS

MI would like to thank Roger de Belsunce, Andrei Cuceu, Shi-Fan Chen and Martin White for enlightening conversations. Numerical calculations have been performed with the Helios cluster at the Insti-

tute for Advanced Study, Princeton and the Baobab high-performance computing cluster at the University of Geneva.

Appendix A: $P^{\rm F}$ analysis

Here we present the results from the Lyα forest auto-power spectrum for various data cut choices.

Fig. 10 illustrates the posterior distribution of the bias parameters. Results are presented for four different $k_{\rm max}$ values: 2, 3, 4, and $5\,h{\rm Mpc}^{-1}$. We see that the posteriors from the $P^{\rm F}$-only analysis with $k_{\rm max} = 2\,h{\rm Mpc}^{-1}$ are fully consistent with those of the baseline 3-spectra analysis. While the Lyα contours for $k_{\rm max} = 3\,h{\rm Mpc}^{-1}$ are entirely consistent with $k_{\rm max} = 2\,h{\rm Mpc}^{-1}$ results, they are inconsistent with the baseline 3-spectra analysis (which uses $k^{\rm F}_{\rm max} = 2\,h{\rm Mpc}^{-1}$). This highlight the importance of multi-tracer analysis in validating scale cuts. For $k_{\rm max} = 4\,h{\rm Mpc}^{-1}$ and $k_{\rm max} = 5\,h{\rm Mpc}^{-1}$, the $P^{\rm F}$-only analysis exhibits significant shifts and a dramatic reduction of the posterior volume.

To evaluate the validity of the perturbation theory, we assess the magnitude of the one-loop correction as a function of wavenumber. Fig. 11 shows the one-loop contribution divided by the tree-level model for the baseline configuration $k_{\rm max} = 2\,h{\rm Mpc}^{-1}$. These results indicates that the perturbative approach is valid up to $k_{\rm max} = 2\,h{\rm Mpc}^{-1}$. Importantly, as shown in ref. [37], for $k_{\rm max} \sim 3\,h{\rm Mpc}^{-1}$, the one-loop corrections is comparable to the tree-level result, suggesting that higher loop corrections may be not negligible. Fitting the $P^{\rm F}$-only data up to $k_{\rm max} = 3\,h{\rm Mpc}^{-1}$ leads to unphysical values of the EFT parameters, which are inconsistent with the results of the $P^{\rm F} + P^{\rm H} + P^{\rm X}$ analysis. The Lyα – all-halo cross-power spectrum effectively break parameter degeneracies, ensuring unbiased inference of the EFT parameters.

Appendix B: $P^{\rm F} + P^{\rm LH} + P^{\rm X}$ analysis with free $c_4^{\rm H}$

In the main analysis, we assume that the c_4 counterterm is universal across all tracers as dictated by the equivalence principle. Here, we consider the extension of the EFT model by introducing one extra parameter c_4^H specific for halos. While this model cannot be considered consistent from the theoretical viewpoint (unless one is willing to violate the equivalence principle), we show here that this allows one to significantly improve the fit quality and push the modeling of the halo auto-power spectrum to smaller scales. Therefore, this extension might have some phenomenological value.

Our EFT model for the Lyα forest and halo auto-power spectra remains unchanged, while for the Lyα – halo cross-power spectra, it modifies to

$$\begin{aligned}
\tilde{P}^{\rm X}_{\text{1-loop}}(k,\mu) &= K_1(\mathbf{k})K_1^{\rm H}(\mathbf{k})P_{\rm lin}(k) \\
&+ 2\int_{\mathbf{q}} K_2(\mathbf{q},\mathbf{k}-\mathbf{q})K_2^{\rm H}(\mathbf{q},\mathbf{k}-\mathbf{q})P_{\rm lin}(|\mathbf{k}-\mathbf{q}|)P_{\rm lin}(q) \\
&+ 3P_{\rm lin}(k)\int_{\mathbf{q}}[K_1(\mathbf{k})K_3^{\rm H}(\mathbf{k},-\mathbf{q},\mathbf{q}) + K_1^{\rm H}(\mathbf{k})K_3(\mathbf{k},-\mathbf{q},\mathbf{q})]P_{\rm lin}(q) \\
&- (c_0 + c_2\mu^2 + c_4\mu^4)K_1^{\rm H}(\mathbf{k})k^2P_{\rm lin}(k) \\
&- (c_0^{\rm H} + c_2^{\rm H}\mu^2 + c_4^{\rm H}\mu^4)K_1(\mathbf{k})k^2P_{\rm lin}(k) \\
&+ P^{\rm X}_{\nabla_z^4\delta}\,,
\end{aligned} \tag{B1}$$

where we introduced a new parameter $c_4^{\rm H}$. In total, the EFT model for the combined 3-spectra analysis features 28 free parameters. For concreteness, we consider the case of light halos. We perform the 3-spectra analysis with the diagonal covariance.

Fig. 12 shows the 1D and 2D posterior distributions for the bias parameters derived from various data combinations. The posteriors of the new 3-spectra analysis are consistent with those from the $P^{\rm F}$-only and $P^{\rm LH}$-only data up to scales of $k^{\rm X}_{\rm max} = 1.5\,h{\rm Mpc}^{-1}$. As $k^{\rm X}_{\rm max}$ increases, the contours shift more gradually compared to the standard analysis in Sec. III B 2, cf. with Fig. 7. As a frequentest confirmation of our results, we observe significantly improved fits across all configurations. For $k^{\rm X}_{\rm max} = 1\,h{\rm Mpc}^{-1}$, the minimum χ^2 value is 376 for 355 data points, indicating a good fit with 28 free parameters. To facilitates a comparison with the results from the standard modeling presented in the main text, we select a conservative scale cut $k^{\rm X}_{\rm max} = 0.8\,h{\rm Mpc}^{-1}$ as a baseline for the 3-spectra analysis.

Tab. III compares the parameter constraints from the baseline 3-spectra analysis for two different EFT models. Although the new framework introduces one additional free parameter, the parameter constraints degrade slightly. The agreement with the results from individual $P^{\rm F}$ and $P^{\rm LH}$ analyses improves significantly for certain EFT parameters. In particular, the $b_2^{\rm LH}$ parameter is in perfect agreement with the peak-background split prediction, $\tilde{b}_2^{\rm LH} = -0.6$ [72], whereas the standard 3-spectra analysis exhibits a 3σ tension with the theoretical pre-

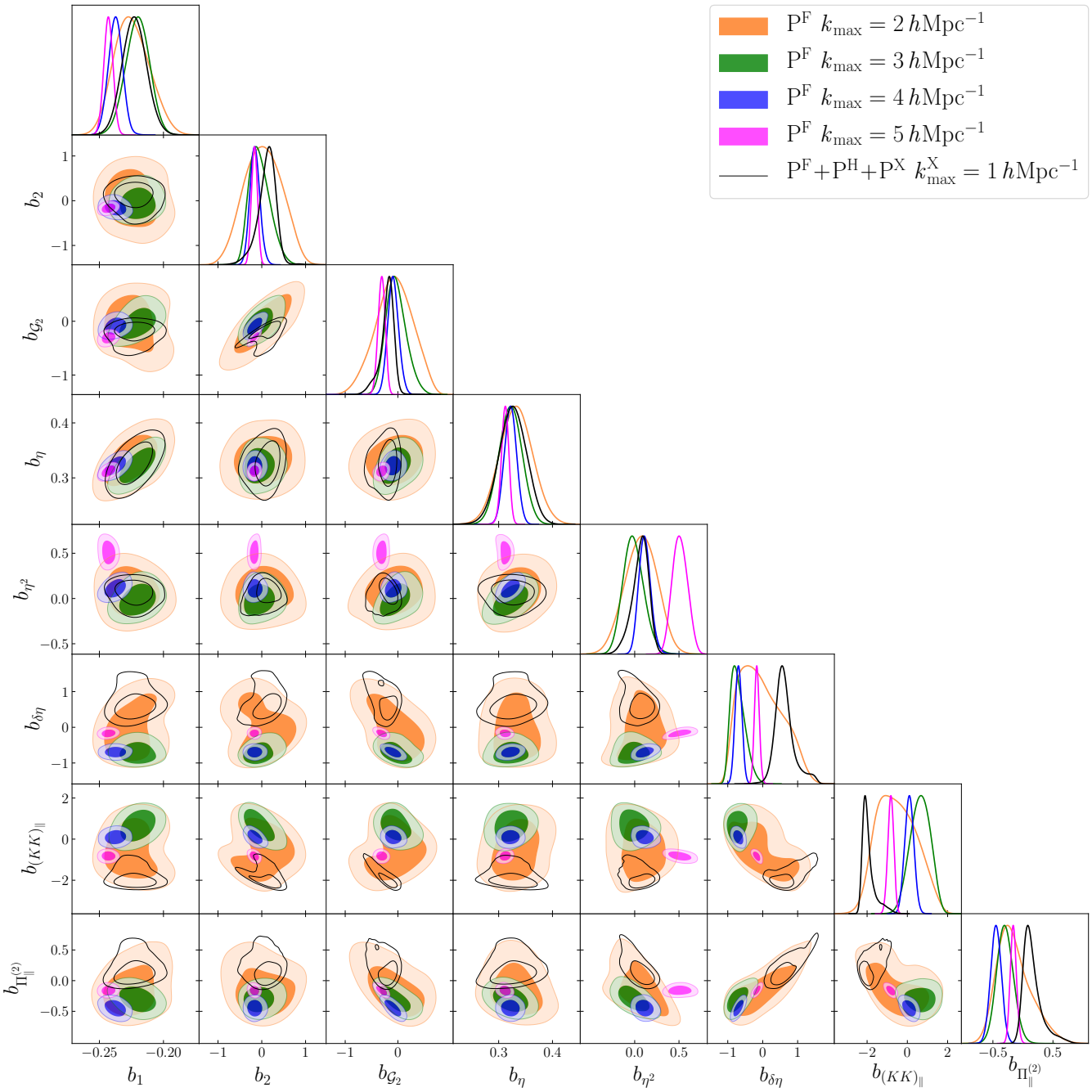

FIG. 10. Marginalized posteriors on nuisance parameters of the EFT model for the Lyα forest auto-power spectrum $P^{\rm F}$ for different values of $k_{\rm max}$: 2, 3, 4 and 5 hMpc^{-1} (orange, green, blue, magenta, respectively). For comparison, the results of the baseline $P^{\rm F} + P^{\rm H} + P^{\rm X}$ analysis with $(k^{\rm F}_{\rm max}, k^{\rm H}_{\rm max}, k^{\rm X}_{\rm max}) = (2, 0.8, 1)\, h$Mpc^{-1} are shown (black).

diction.

We evaluate the performance of the extended EFT model. Our best-fit prediction describes the $P^{\rm F}$, $P^{\rm LH}$ and $P^{\rm X}$ data at $(k^{\rm F}_{\rm max}, k^{\rm H}_{\rm max}, k^{\rm X}_{\rm max}) = (2, 0.8, 1)\, h$Mpc^{-1} with 0.8%, 2.5% and 0.8% accuracy, respectively. This represents a substantial improvement in the modeling of the halo power spectrum compared to the baseline 3-spectra analysis, which achieved 3.4% accuracy. Fig. 13 showcase the performance of our new model for the $P^{\rm LH}$ spectrum, cf. with Fig. 8. No significant improvement was observed in the modeling of the $P^{\rm F}$ and $P^{\rm X}$ data.

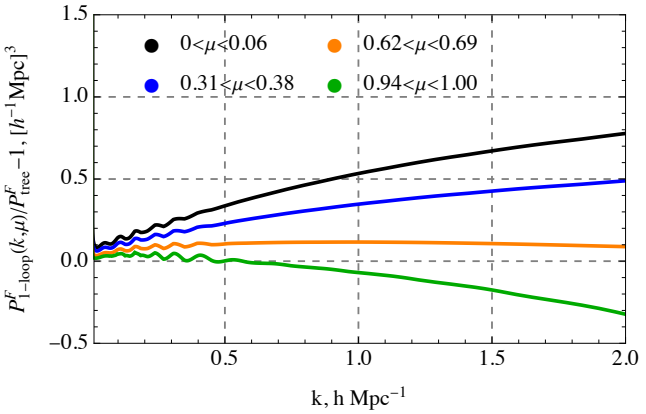

FIG. 11. The magnitude of one-loop corrections relative to the linear theory prediction for the Lyα forest auto-power spectrum. The theory prediction is based on the best-fit model with $k_{\rm max} = 2\,h{\rm Mpc}^{-1}$.

[1] U. Seljak, A. Makarov, P. McDonald, S. F. Anderson, N. A. Bahcall, J. Brinkmann et al., *Cosmological parameter analysis including SDSS Lyα forest and galaxy bias: Constraints on the primordial spectrum of fluctuations, neutrino mass, and dark energy*, *Phys. Rev. D* **71** (2005) 103515 [astro-ph/0407372].

[2] M. Viel, M. G. Haehnelt and V. Springel, *The effect of neutrinos on the matter distribution as probed by the intergalactic medium*, *J. Cosmology Astropart. Phys.* **2010** (2010) 015 [1003.2422].

[3] N. Palanque-Delabrouille, C. Yèche, A. Borde, J.-M. Le Goff, G. Rossi, M. Viel et al., *The one-dimensional Lyα forest power spectrum from BOSS*, *A&A* **559** (2013) A85 [1306.5896].

[4] N. Palanque-Delabrouille, C. Yèche, N. Schöneberg, J. Lesgourgues, M. Walther, S. Chabanier et al., *Hints, neutrino bounds, and WDM constraints from SDSS DR14 Lyman-α and Planck full-survey data*, *J. Cosmology Astropart. Phys.* **2020** (2020) 038 [1911.09073].

[5] N. Afshordi, P. McDonald and D. N. Spergel, *Primordial Black Holes as Dark Matter: The Power Spectrum and Evaporation of Early Structures*, *ApJ* **594** (2003) L71 [astro-ph/0302035].

[6] R. Murgia, G. Scelfo, M. Viel and A. Raccanelli, *Lyman-α Forest Constraints on Primordial Black Holes as Dark Matter*, *Phys. Rev. Lett.* **123** (2019) 071102 [1903.10509].

[7] M. Viel, G. D. Becker, J. S. Bolton and M. G. Haehnelt, *Warm dark matter as a solution to the small scale crisis: New constraints from high redshift Lyman-α forest data*, *Phys. Rev. D* **88** (2013) 043502 [1306.2314].

[8] J. Baur, N. Palanque-Delabrouille, C. Yèche, C. Magneville and M. Viel, *Lyman-alpha forests cool warm dark matter*, *J. Cosmology Astropart. Phys.* **2016** (2016) 012 [1512.01981].

[9] V. Iršič, M. Viel, M. G. Haehnelt, J. S. Bolton, S. Cristiani, G. D. Becker et al., *New Constraints on the free-streaming of warm dark matter from intermediate and small scale Lyman-α forest data*, *ArXiv e-prints* (2017) [1702.01764].

[10] T. Kobayashi, R. Murgia, A. De Simone, V. Iršič and M. Viel, *Lyman-α constraints on ultralight scalar dark matter: Implications for the early and late universe*, *Phys. Rev. D* **96** (2017) 123514 [1708.00015].

[11] E. Armengaud, N. Palanque-Delabrouille, C. Yèche, D. J. E. Marsh and J. Baur, *Constraining the mass of light bosonic dark matter using SDSS Lyman-α forest*, *MNRAS* **471** (2017) 4606 [1703.09126].

[12] R. Murgia, V. Iršič and M. Viel, *Novel constraints on noncold, nonthermal dark matter from Lyman-α forest data*, *Phys. Rev. D* **98** (2018) 083540 [1806.08371].

[13] A. Garzilli, A. Magalich, T. Theuns, C. S. Frenk, C. Weniger, O. Ruchayskiy et al., *The Lyman-α forest as a diagnostic of the nature of the dark matter*, *MNRAS* **489** (2019) 3456 [1809.06585].

[14] V. Iršič, H. Xiao and M. McQuinn, *Early structure formation constraints on the ultralight axion in the postinflation scenario*, *Phys. Rev. D* **101** (2020) 123518 [1911.11150].

[15] K. K. Rogers, C. Dvorkin and H. V. Peiris, *Limits on the Light Dark Matter-Proton Cross Section from Cosmic Large-Scale Structure*, *Phys. Rev. Lett.* **128** (2022) 171301 [2111.10386].

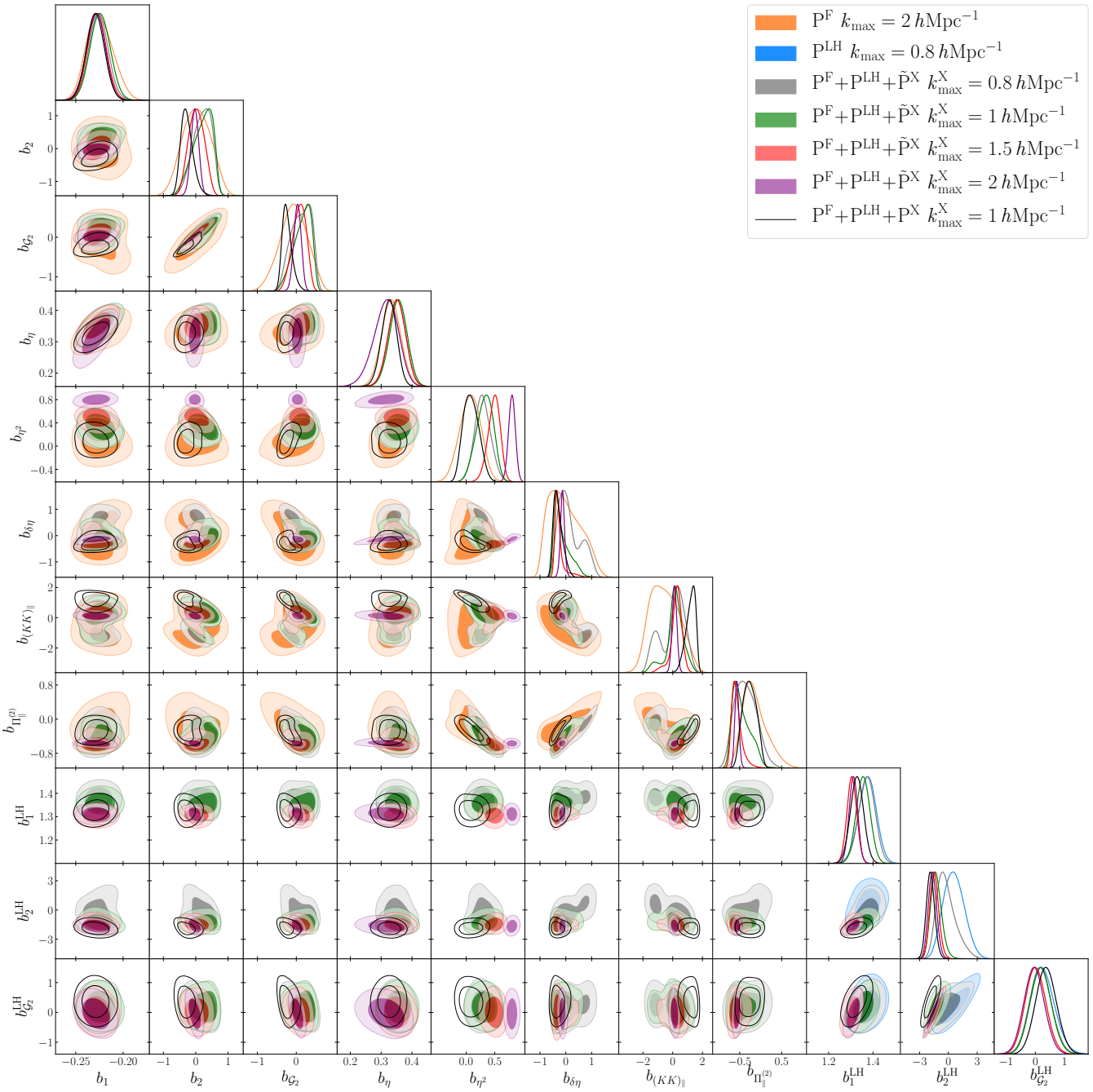

FIG. 12. Marginalized posteriors on nuisance parameters of the EFT model for the Lyα forest auto-power spectrum $P^{\rm F}$ (orange), the all-halo auto-power spectrum $P^{\rm LH}$ (blue), and their combination with the Lyα – all-halo cross-power spectrum $\tilde{P}^{\rm X}$ at $z = 2.8$. Here, the tilde symbol in $\tilde{P}^{\rm X}$ emphasizes that a different model for the cross-power spectrum, as defined in (B1), is employed. The combined analysis results are shown for four different values of $k^{\rm X}_{\rm max}$: 0.8, 1, 1.5, and 2 hMpc^{-1} (gray, green, red, purple, respectively). All results are obtained with the diagonal covariance.

[16] B. Villasenor, B. Robertson, P. Madau and E. Schneider, *New constraints on warm dark matter from the Lyman-α forest power spectrum*, *Phys. Rev. D* **108** (2023) 023502 [2209.14220].

[17] V. Iršič, M. Viel, M. G. Haehnelt, J. S. Bolton, M. Molaro, E. Puchwein et al., *Unveiling Dark Matter free-streaming at the smallest scales with high redshift Lyman-alpha forest*, *arXiv e-prints* (2023) arXiv:2309.04533 [2309.04533].

[18] S. Goldstein, J. C. Hill, V. Iršič and B. D. Sherwin,

Param. \ Data	$P^{\rm F}$	$P^{\rm LH}$	$P^{\rm F}+P^{\rm LH}+P^{\rm X}$	$P^{\rm F}+P^{\rm LH}+\tilde{P}^{\rm X}$
b_1	$-0.2245^{+0.0126}_{-0.0154}$	–	$-0.2291^{+0.0095}_{-0.0098}$	$-0.2241^{+0.0107}_{-0.0107}$
b_η	$0.332^{-0.031}_{-0.031}$	–	$0.326^{+0.026}_{-0.024}$	$0.355^{+0.030}_{-0.028}$
b_2	$0.03^{+0.44}_{-0.46}$	–	$-0.27^{+0.15}_{-0.22}$	$0.21^{+0.40}_{-0.22}$
$b_{\mathcal{G}_2}$	$-0.07^{+0.38}_{-0.34}$	–	$-0.24^{+0.09}_{-0.15}$	$0.16^{+0.29}_{-0.15}$
b_{η^2}	$0.072^{+0.194}_{-0.180}$	–	$-0.087^{+0.126}_{-0.154}$	$0.325^{+0.167}_{-0.136}$
$b_{\delta\eta}$	$-0.03^{+0.42}_{-0.83}$	–	$-0.30^{+0.13}_{-0.22}$	$-0.15^{+0.13}_{-0.38}$
$b_{(KK)_\parallel}$	$-0.51^{+0.86}_{-1.18}$	–	$1.20^{+0.41}_{-0.23}$	$0.14^{+0.58}_{-0.41}$
$b_{\Pi^{[2]}_\parallel}$	$-0.142^{+0.212}_{-0.350}$	–	$-0.266^{+0.166}_{-0.175}$	$-0.459^{+0.137}_{-0.272}$
b_{Γ_3}	$-0.49^{+0.13}_{-0.13}$	–	$-0.32^{+0.11}_{-0.11}$	$-1.31^{+0.11}_{-0.11}$
$10^2 c_0/[h^{-1}\mathrm{Mpc}]^2$	$-2.32^{+1.06}_{-1.06}$	–	$-2.66^{+0.65}_{-0.65}$	$-1.85^{+0.61}_{-0.61}$
$10^2 c_2/[h^{-1}\mathrm{Mpc}]^2$	$4.26^{+1.54}_{-1.54}$	–	$3.50^{+1.20}_{-1.20}$	$2.89^{+1.20}_{-1.20}$
$10^2 c_4/[h^{-1}\mathrm{Mpc}]^2$	$-5.38^{+1.0}_{-1.0}$	–	$-3.03^{+0.90}_{-0.90}$	$-4.77^{+0.91}_{-0.91}$
$b_{\Pi^{[3]}_\parallel}$	$0.771^{+0.089}_{-0.089}$	–	$0.931^{+0.085}_{-0.085}$	$1.228^{+0.085}_{-0.085}$
$b_{\delta\Pi^{[2]}_\parallel}$	$-0.05^{+0.19}_{-0.19}$	–	$-0.17^{+0.18}_{-0.18}$	$-1.20^{+0.18}_{-0.18}$
$b_{(K\Pi^{[2]})_\parallel}$	$-1.64^{+0.25}_{-0.25}$	–	$-3.07^{+0.20}_{-0.20}$	$-2.79^{+0.20}_{-0.20}$
$b_{\eta\Pi^{[2]}_\parallel}$	$-0.24^{+0.43}_{-0.43}$	–	$0.54^{+0.42}_{-0.42}$	$0.23^{+0.42}_{-0.42}$
$b_1^{\rm LH}$	–	$1.375^{+0.042}_{-0.039}$	$1.327^{+0.030}_{-0.030}$	$1.355^{+0.032}_{-0.032}$
$b_2^{\rm LH}$	–	$0.58^{+1.03}_{-1.20}$	$-1.86^{+0.41}_{-0.46}$	$-1.26^{+0.51}_{-0.64}$
$b_{\mathcal{G}_2}^{\rm LH}$	–	$0.25^{+0.39}_{-0.44}$	$0.37^{+0.37}_{-0.37}$	$0.19^{+0.36}_{-0.37}$
$b_{\Gamma_3}^{\rm LH}$	–	$0.14^{+0.13}_{-0.13}$	$-0.18^{+0.08}_{-0.08}$	$0.0^{+0.09}_{-0.09}$
$c_0^{\rm LH}/[h^{-1}\mathrm{Mpc}]^2$	–	$0.024^{+0.087}_{-0.087}$	$-0.196^{+0.051}_{-0.051}$	$-0.252^{+0.055}_{-0.055}$
$c_2^{\rm LH}/[h^{-1}\mathrm{Mpc}]^2$	–	$1.404^{+0.159}_{-0.159}$	$-0.240^{+0.065}_{-0.065}$	$0.153^{+0.095}_{-0.095}$
$c_4^{\rm LH}/[h^{-1}\mathrm{Mpc}]^2$	–	$2.15^{+0.42}_{-0.42}$	–	$1.53^{+0.23}_{-0.23}$
$\tilde{c}^{\rm LH}/[h^{-1}\mathrm{Mpc}]^4$	–	$-0.81^{+0.77}_{-0.77}$	$3.53^{+0.22}_{-0.22}$	$0.66^{+0.41}_{-0.41}$
$P_{\rm shot}^{\rm LH}$	–	$0.001^{+1.0}_{-1.0}$	$-0.24^{+0.95}_{-0.95}$	$-0.14^{+0.94}_{-0.94}$
$a_0^{\rm LH}$	–	$0.0^{+1.0}_{-1.0}$	$0.0^{+1.0}_{-1.0}$	$-0.01^{+1.0}_{-1.0}$
$a_2^{\rm LH}$	–	$0.0^{+1.0}_{-1.0}$	$0.0^{+1.0}_{-1.0}$	$0.0^{+1.0}_{-1.0}$
$\tilde{c}^{\rm X}/[h^{-1}\mathrm{Mpc}]^4$	–	–	$0.623^{+0.049}_{-0.049}$	$-0.044^{+0.107}_{-0.107}$

TABLE III. One-dimensional marginalized constraints on nuisance parameters of the one-loop EFT model from the Lyα forest auto-power spectrum with $k^{\rm F}_{\rm max} = 2\ h\mathrm{Mpc}^{-1}$ (second column), the all-halo auto-power spectrum with $k^{\rm H}_{\rm max} = 0.8\ h\mathrm{Mpc}^{-1}$ (third column) and their combination with the Lyα – all-halo cross-power spectrum with $k^{\rm X}_{\rm max} = 1\ h\mathrm{Mpc}^{-1}$ using two different EFT model for the cross-power spectrum at $z = 2.8$. All results are obtained with the diagonal covariance. Parameter constraints related to each respective spectrum are grouped together. The parameters in the upper section were directly sampled in our MCMC chains, while the parameters in the lower section were analytically marginalized in the likelihood, with their posteriors recovered from the chains *a posteriori*.

Canonical Hubble-Tension-Resolving Early Dark Energy Cosmologies Are Inconsistent with the Lyman-α Forest, *Phys. Rev. Lett.* **131** (2023) 201001 [2303.00746].

[19] P. McDonald and D. J. Eisenstein, *Dark energy and curvature from a future baryonic acoustic oscillation survey using the Lyman-α forest*, *Phys. Rev. D* **76** (2007) 063009 [astro-ph/0607122].

[20] A. Slosar, V. Iršič, D. Kirkby, S. Bailey, N. G. Busca, T. Delubac et al., *Measurement of baryon acoustic oscillations in the Lyman-α forest fluctuations in BOSS data release 9*, *J. Cosmology Astropart. Phys.* **2013** (2013) 026 [1301.3459].

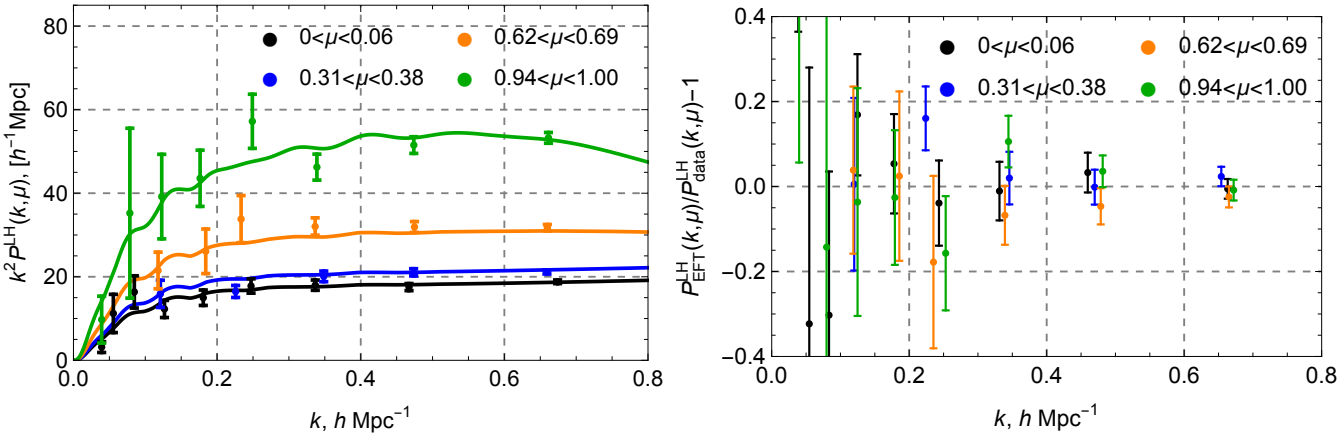

FIG. 13. Best-fit EFT predictions for the light-halo power spectrum against the simulated data (left panel) and the residuals between the model and the data (right panel). The best-fit model was obtained in the $P^{\rm F} + P^{\rm LH} + \tilde{P}^{\rm X}$ analysis with $(k^{\rm F}_{\rm max}, k^{\rm H}_{\rm max}, k^{\rm X}_{\rm max}) = (2, 0.8, 1)\, h{\rm Mpc}^{-1}$.

[21] N. G. Busca, T. Delubac, J. Rich, S. Bailey, A. Font-Ribera, D. Kirkby et al., *Baryon acoustic oscillations in the Lyα forest of BOSS quasars*, *A&A* **552** (2013) A96 [1211.2616].

[22] H. du Mas des Bourboux et al., *The Completed SDSS-IV Extended Baryon Oscillation Spectroscopic Survey: Baryon Acoustic Oscillations with Lyα Forests*, *Astrophys. J.* **901** (2020) 153 [2007.08995].

[23] DESI Collaboration, A. G. Adame, J. Aguilar, S. Ahlen, S. Alam, D. M. Alexander et al., *DESI 2024 IV: Baryon Acoustic Oscillations from the Lyman Alpha Forest*, *arXiv e-prints* (2024) arXiv:2404.03001 [2404.03001].

[24] A. Font-Ribera et al., *The large-scale Quasar-Lyman \alpha\ Forest Cross-Correlation from BOSS*, *JCAP* **05** (2013) 018 [1303.1937].

[25] BOSS collaboration, A. Font-Ribera et al., *Quasar-Lyman α Forest Cross-Correlation from BOSS DR11 : Baryon Acoustic Oscillations*, *JCAP* **05** (2014) 027 [1311.1767].

[26] F. Gerardi, A. Cuceu, A. Font-Ribera, B. Joachimi and P. Lemos, *Direct cosmological inference from three-dimensional correlations of the Lyman α forest*, *Mon. Not. Roy. Astron. Soc.* **518** (2022) 2567 [2209.11263].

[27] A. Cuceu, A. Font-Ribera, B. Joachimi and S. Nadathur, *Cosmology beyond BAO from the 3D distribution of the Lyman-α forest*, *Mon. Not. Roy. Astron. Soc.* **506** (2021) 5439 [2103.14075].

[28] D. Baumann, A. Nicolis, L. Senatore and M. Zaldarriaga, *Cosmological Non-Linearities as an Effective Fluid*, *JCAP* **1207** (2012) 051 [1004.2488].

[29] J. J. M. Carrasco, M. P. Hertzberg and L. Senatore, *The Effective Field Theory of Cosmological Large Scale Structures*, *JHEP* **09** (2012) 082 [1206.2926].

[30] M. M. Ivanov, *Effective Field Theory for Large-Scale Structure*. 2023. 2212.08488.

[31] M. M. Ivanov, M. Simonović and M. Zaldarriaga, *Cosmological Parameters from the BOSS Galaxy Power Spectrum*, *JCAP* **05** (2020) 042 [1909.05277].

[32] G. D'Amico, J. Gleyzes, N. Kokron, D. Markovic, L. Senatore, P. Zhang et al., *The Cosmological Analysis of the SDSS/BOSS data from the Effective Field Theory of Large-Scale Structure*, 1909.05271.

[33] S.-F. Chen, Z. Vlah and M. White, *A new analysis of galaxy 2-point functions in the BOSS survey, including full-shape information and post-reconstruction BAO*, *JCAP* **02** (2022) 008 [2110.05530].

[34] A. Chudaykin and M. M. Ivanov, *Cosmological constraints from the power spectrum of eBOSS quasars*, *Phys. Rev. D* **107** (2023) 043518 [2210.17044].

[35] S.-F. Chen, M. M. Ivanov, O. H. E. Philcox and L. Wenzl, *Suppression without Thawing: Constraining Structure Formation and Dark Energy with Galaxy Clustering*, *Phys. Rev. Lett.* **133** (2024) 231001 [2406.13388].

[36] DESI collaboration, A. G. Adame et al., *DESI 2024 VII: Cosmological Constraints from the Full-Shape Modeling of Clustering Measurements*, 2411.12022.

[37] M. M. Ivanov, *Lyman alpha forest power spectrum in effective field theory*, *Phys. Rev. D* **109** (2024) 023507 [2309.10133].

[38] V. Desjacques, D. Jeong and F. Schmidt, *The Galaxy Power Spectrum and Bispectrum in Redshift Space*, *JCAP* **1812** (2018) 035 [1806.04015].

[39] M. Garny, T. Konstandin, L. Sagunski and S. Tulin, *Lyman-α forest constraints on interacting dark sectors*, *JCAP* **09** (2018) 011 [1805.12203].

[40] M. Garny, T. Konstandin, L. Sagunski and M. Viel,

Neutrino mass bounds from confronting an effective model with BOSS Lyman-α data, *JCAP* **03** (2021) 049 [2011.03050].

[41] S.-F. Chen, Z. Vlah and M. White, *The Lyα forest flux correlation function: a perturbation theory perspective*, *JCAP* **05** (2021) 053 [2103.13498].

[42] J. J. Givans and C. M. Hirata, *Redshift-space streaming velocity effects on the Lyman-α forest baryon acoustic oscillation scale*, *Phys. Rev. D* **102** (2020) 023515 [2002.12296].

[43] J. J. Givans, A. Font-Ribera, A. Slosar, L. Seeyave, C. Pedersen, K. K. Rogers et al., *Non-linearities in the Lyman-α forest and in its cross-correlation with dark matter halos*, *JCAP* **09** (2022) 070 [2205.00962].

[44] B. Abareshi, J. Aguilar, S. Ahlen, S. Alam, D. M. Alexander, R. Alfarsy et al., *Overview of the Instrumentation for the Dark Energy Spectroscopic Instrument*, *arXiv e-prints* (2022) arXiv:2205.10939 [2205.10939].

[45] C. Gordon et al., *3D Correlations in the Lyman-α Forest from Early DESI Data*, *JCAP* **11** (2023) 045 [2308.10950].

[46] J. S. Bolton, E. Puchwein, D. Sijacki, M. G. Haehnelt, T.-S. Kim, A. Meiksin et al., *The Sherwood simulation suite: overview and data comparisons with the Lyman α forest at redshifts 2 ≤ z ≤ 5*, *Mon. Not. Roy. Astron. Soc.* **464** (2017) 897 [1605.03462].

[47] J. Ravi, B. Hadzhiyska, M. J. White, L. Hernquist and S. Bose, *Examining Lyman-alpha emitters through simulations in anticipation of the DESI-II survey*, *Phys. Rev. D* **110** (2024) 103509 [2403.02414].

[48] D. Wadekar and R. Scoccimarro, *The Galaxy Power Spectrum Multipoles Covariance in Perturbation Theory*, 1910.02914.

[49] D. Wadekar, M. M. Ivanov and R. Scoccimarro, *Cosmological constraints from BOSS with analytic covariance matrices*, *Phys. Rev. D* **102** (2020) 123521 [2009.00622].

[50] O. H. E. Philcox, M. M. Ivanov, M. Zaldarriaga, M. Simonovic and M. Schmittfull, *Fewer Mocks and Less Noise: Reducing the Dimensionality of Cosmological Observables with Subspace Projections*, *Phys. Rev. D* **103** (2021) 043508 [2009.03311].

[51] T. Baldauf, M. Mirbabayi, M. Simonović and M. Zaldarriaga, *LSS constraints with controlled theoretical uncertainties*, 1602.00674.

[52] A. Chudaykin and M. M. Ivanov, *Measuring neutrino masses with large-scale structure: Euclid forecast with controlled theoretical error*, *JCAP* **11** (2019) 034 [1907.06666].

[53] A. Chudaykin, M. M. Ivanov and M. Simonović, *Optimizing large-scale structure data analysis with the theoretical error likelihood*, *Phys. Rev. D* **103** (2021) 043525 [2009.10724].

[54] S. Chabanier, N. Palanque-Delabrouille, C. Yèche, J.-M. Le Goff, E. Armengaud, J. Bautista et al., *The one-dimensional power spectrum from the SDSS DR14 Lyα forests*, *J. Cosmology Astropart. Phys.* **2019** (2019) 017 [1812.03554].

[55] M. M. Ivanov, M. W. Toomey and N. G. Karaçaylı, *Fundamental physics with the Lyman-alpha forest: constraints on the growth of structure and neutrino masses from SDSS with effective field theory*, 2405.13208.

[56] R. de Belsunce, S.-F. Chen, M. M. Ivanov, C. Ravoux, S. Chabanier, J. Sexton et al., *The ACCEL2 Project: Precision Measurements of EFT Parameters and BAO Peak Shifts for the Lyman-α Forest*, 2412.06892.

[57] P. Taule and M. Garny, *The two-loop power spectrum in redshift space*, *JCAP* **11** (2023) 078 [2308.07379].

[58] A. Chudaykin, M. M. Ivanov, O. H. E. Philcox and M. Simonović, *Nonlinear perturbation theory extension of the Boltzmann code CLASS*, *Phys. Rev. D* **102** (2020) 063533 [2004.10607].

[59] M. Simonović, T. Baldauf, M. Zaldarriaga, J. J. Carrasco and J. A. Kollmeier, *Cosmological perturbation theory using the FFTLog: formalism and connection to QFT loop integrals*, *JCAP* **1804** (2018) 030 [1708.08130].

[60] D. Blas, M. Garny, M. M. Ivanov and S. Sibiryakov, *Time-Sliced Perturbation Theory for Large Scale Structure I: General Formalism*, *JCAP* **1607** (2016) 052 [1512.05807].

[61] D. Blas, M. Garny, M. M. Ivanov and S. Sibiryakov, *Time-Sliced Perturbation Theory II: Baryon Acoustic Oscillations and Infrared Resummation*, *JCAP* **1607** (2016) 028 [1605.02149].

[62] M. M. Ivanov and S. Sibiryakov, *Infrared Resummation for Biased Tracers in Redshift Space*, *JCAP* **1807** (2018) 053 [1804.05080].

[63] M. McQuinn and M. White, *On Estimating Lyman-alpha Forest Correlations between Multiple Sightlines*, *Mon. Not. Roy. Astron. Soc.* **415** (2011) 2257 [1102.1752].

[64] A. Chudaykin, K. Dolgikh and M. M. Ivanov, *Constraints on the curvature of the Universe and dynamical dark energy from the Full-shape and BAO data*, *Phys. Rev. D* **103** (2021) 023507 [2009.10106].

[65] A. Perko, L. Senatore, E. Jennings and R. H. Wechsler, *Biased Tracers in Redshift Space in the EFT of Large-Scale Structure*, 1610.09321.

[66] M. M. Ivanov, A. Obuljen, C. Cuesta-Lazaro and M. W. Toomey, *Full-shape analysis with simulation-based priors: cosmological parameters and the structure growth anomaly*, 2409.10609.

[67] eBOSS collaboration, G.-B. Zhao et al., *The completed*

SDSS-IV extended Baryon Oscillation Spectroscopic Survey: a multitracer analysis in Fourier space for measuring the cosmic structure growth and expansion rate, *Mon. Not. Roy. Astron. Soc.* **504** (2021) 33 [2007.09011].

[68] T. Mergulhão, H. Rubira, R. Voivodic and L. R. Abramo, *The effective field theory of large-scale structure and multi-tracer*, *JCAP* **04** (2022) 021 [2108.11363].

[69] B. Audren, J. Lesgourgues, K. Benabed and S. Prunet, *Conservative Constraints on Early Cosmology: an illustration of the Monte Python cosmological parameter inference code*, *JCAP* **1302** (2013) 001 [1210.7183].

[70] T. Brinckmann and J. Lesgourgues, *MontePython 3: boosted MCMC sampler and other features*, *Phys. Dark Univ.* **24** (2019) 100260 [1804.07261].

[71] A. Lewis, *GetDist: a Python package for analysing Monte Carlo samples*, 1910.13970.

[72] T. Lazeyras, C. Wagner, T. Baldauf and F. Schmidt, *Precision measurement of the local bias of dark matter halos*, *JCAP* **1602** (2016) 018 [1511.01096].

[73] M. M. Ivanov et al., *The Millennium and Astrid galaxies in effective field theory: comparison with galaxy-halo connection models at the field level*, 2412.01888.

[74] J. C. Jackson, *Fingers of God: A critique of Rees' theory of primoridal gravitational radiation*, *Mon. Not. Roy. Astron. Soc.* **156** (1972) 1P [0810.3908].

[75] P. S. Behroozi, R. H. Wechsler and H.-Y. Wu, *The ROCKSTAR Phase-space Temporal Halo Finder and the Velocity Offsets of Cluster Cores*, *ApJ* **762** (2013) 109 [1110.4372].

[76] B. Hadzhiyska, D. Eisenstein, S. Bose, L. H. Garrison and N. Maksimova, *compaso: A new halo finder for competitive assignment to spherical overdensities*, *Mon. Not. Roy. Astron. Soc.* **509** (2021) 501 [2110.11408].

[77] M. Schmittfull, M. Simonović, M. M. Ivanov, O. H. E. Philcox and M. Zaldarriaga, *Modeling Galaxies in Redshift Space at the Field Level*, 2012.03334.

[78] M. M. Ivanov, C. Cuesta-Lazaro, S. Mishra-Sharma, A. Obuljen and M. W. Toomey, *Full-shape analysis with simulation-based priors: Constraints on single field inflation from BOSS*, *Phys. Rev. D* **110** (2024) 063538 [2402.13310].

[79] S. Chabanier, C. Ravoux, L. Latrille, J. Sexton, E. Armengaud, J. Bautista et al., *The ACCEL^2 project: simulating Lyman-α forest in large-volume hydrodynamical simulations*, 2407.04473.

[80] M. Peloso and M. Pietroni, *Galilean invariance and the consistency relation for the nonlinear squeezed bispectrum of large scale structure*, *JCAP* **05** (2013) 031 [1302.0223].

[81] A. Kehagias and A. Riotto, *Symmetries and Consistency Relations in the Large Scale Structure of the Universe*, *Nucl. Phys. B* **873** (2013) 514 [1302.0130].

[82] P. Valageas and T. Nishimichi, *Combining perturbation theories with halo models for the matter bispectrum*, *Astronomy & Astrophysics* **532** (2011) A4 [1102.0641].

[83] P. Creminelli, J. Noreña, M. Simonović and F. Vernizzi, *Single-Field Consistency Relations of Large Scale Structure*, *JCAP* **12** (2013) 025 [1309.3557].

[84] P. Creminelli, J. Gleyzes, L. Hui, M. Simonović and F. Vernizzi, *Single-Field Consistency Relations of Large Scale Structure. Part III: Test of the Equivalence Principle*, *JCAP* **06** (2014) 009 [1312.6074].

[85] P. Creminelli, J. Gleyzes, M. Simonović and F. Vernizzi, *Single-Field Consistency Relations of Large Scale Structure. Part II: Resummation and Redshift Space*, *JCAP* **02** (2014) 051 [1311.0290].

[86] D. Blas, M. M. Ivanov and S. Sibiryakov, *Testing Lorentz invariance of dark matter*, *JCAP* **10** (2012) 057 [1209.0464].

[87] B. Audren, D. Blas, M. M. Ivanov, J. Lesgourgues and S. Sibiryakov, *Cosmological constraints on deviations from Lorentz invariance in gravity and dark matter*, *JCAP* **03** (2015) 016 [1410.6514].